Remote Sensing of Environment 282 (2022) 113283

Contents lists available at ScienceDirect

Remote Sensing of Environment

journal homepage: www.elsevier.com/locate/rse

Evaluation of satellite and reanalysis estimates of surface and root-zone soil moisture in croplands of Jiangsu Province, China

Lei Fan [a], Zanpin Xing [b,c,*], Gabrielle De Lannoy [d], Frédéric Frappart [e,f], Jian Peng [g,h], Jiangyuan Zeng [i], Xiaojun Li [j], Kun Yang [k,l], Tianjie Zhao [i], Jiancheng Shi [i], Hongliang Ma [j,m], Mengjia Wang [j], Xiangzhuo Liu [j], Chuanxiang Yi [n], Mingguo Ma [a], Xuguang Tang [a], Jianguang Wen [i], Xiuzhi Chen [o], Chong Wang [p], Lingxiao Wang [p], Guojie Wang [p], Jean-Pierre Wigneron [j]

[a] Chongqing Jinfo Mountain Karst Ecosystem National Observation and Research Station, School of Geographical Sciences, Southwest University, Chongqing 400715, China
[b] Cryosphere Research Station on the Qinghai-Tibet Plateau, State Key Laboratory of Cryospheric Science, Northwest Institute of Eco-Environment and Resource, Chinese Academy of Sciences, Lanzhou, Gansu 730000, China
[c] University of Chinese Academy of Sciences, Beijing 100049, China
[d] Department of Earth and Environmental Sciences, KU Leuven, Heverlee B-3001, Belgium
[e] Laboratoire d'Etudes en Géophysique et Océanographie Spatiales (LEGOS), Université de Toulouse, 31400 Toulouse, France
[f] Géosciences Environnement Toulouse (GET), 31400 Toulouse, France
[g] Department of Remote Sensing, Helmholtz Centre for Environmental Research–UFZ, Permoserstrasse 15, 04318 Leipzig, Germany
[h] Remote Sensing Centre for Earth System Research, Leipzig University, 04103 Leipzig, Germany
[i] State Key Laboratory of Remote Sensing Science, Aerospace Information Research Institute, Chinese Academy of Sciences, Beijing 100101, China
[j] INRAE, UMR1391 ISPA, Université de Bordeaux, France
[k] Ministry of Education Key Laboratory for Earth System Modeling, Department of Earth System Science, Tsinghua University, Beijing, 100084, China
[l] Center for Excellence in Tibetan Plateau Earth Sciences, Institute of Tibetan Plateau Research, Chinese Academy of Sciences, Beijing 100101, China
[m] State Key Laboratory of Information Engineering in Surveying, Mapping, and Remote Sensing, Wuhan University, Wuhan 430079, China
[n] Yancheng Meteorological Observatory, Yancheng 224005, China
[o] School of Atmospheric Sciences, Center for Monsoon and Environment Research, Sun Yat-Sen University, Guangzhou, China
[p] School of Geographical Sciences, Nanjing University of Information Science & Technology, Nanjing 210044, China

ARTICLE INFO

Edited by Jing M. Chen

Keywords:
Jiangsu province
Microwave remote sensing
Reanalysis datasets
Surface soil moisture
Root-zone soil moisture
Evaluation strategies
Inter-comparison
Triple collocation

ABSTRACT

High-quality and long-term surface soil moisture (SSM) and root-zone soil moisture (RZSM) data are critical for agricultural water management of Jiangsu province, which is a major agricultural province in China. However, few studies assessed the accuracy of SSM and RZSM datasets in croplands of Jiangsu province. The study addressed this gap by firstly using observations from ninety-one sites to assess thirteen satellite and model-based SSM products (Advanced Scatterometer (ASCAT), European Space Agency Climate Change Initiative (ESA CCI) Combined/Passive/Active, Soil Moisture and Ocean Salinity in version IC (SMOS-IC), Land Parameter Retrieval Model (LPRM) Advanced Microwave Scanning Radiometer 2 (AMSR2), Soil Moisture Active Passive (SMAP)-Multi-Temporal Dual-channel Algorithm (MTDCA)/Level 3 (L3)/Level 4 (L4)/SMAP-INRAE-BORDEAUX (IB)/Multi-channel Collaborative Algorithm (MCCA), the fifth generation of the land component of the European Centre for Medium-Range Weather Forecasts atmospheric reanalysis (ERA5-Land), and the Noah land surface model driven by Global Land Data Assimilation System (GLDAS-Noah)), and four RZSM products (ERA5-Land, GLDAS-Noah, SMAP-L4 and ESA CCI (retrieved using ESA CCI Combined SSM coupled with an exponential filter)). We also inter-compared time-invariant and time-variant Triple Collocation Analysis (TCA)-based *R* with *in situ*-based *R* calculated using SSM anomalies. Various evaluation strategies were compared using different groups of available sites and temporal samplings. Our results showed that the model-based and combined SSM products (*i.e.*, ERA5-Land, SMAP-L4, ESA CCI Combined/Passive/Active, GLDAS-Noah, ASCAT) performed better than the other SSM products and ERA5-Land, SMAP-L4 and ESA CCI RZSM generally performed better than the

* Corresponding author at: Cryosphere Research Station on the Qinghai-Tibet Plateau, State Key Laboratory of Cryospheric Science, Northwest Institute of Eco-Environment and Resource, Chinese Academy of Sciences, Lanzhou, Gansu 730000, China.
E-mail address: xingzp@lzb.ac.cn (Z. Xing).

https://doi.org/10.1016/j.rse.2022.113283
Received 15 March 2022; Received in revised form 9 September 2022; Accepted 17 September 2022
Available online 26 September 2022

GLDAS-Noah RZSM product with higher *R*. Similar performance rankings were observed among time-invariant and time-variant TCA-*R* and *in situ*-based *R*, in which the TCA-*R* values for all SSM datasets were higher than the *in situ*-based *R* as the representativeness errors of the *in situ* measurements may bias *in situ*-based *R*. The accuracy of the ESA CCI, GLDAS-Noah and ERA5-Land SSM products was expected to be enhanced by considering the water effect and high uncertainties were observed for MTDCA and SMAP-MCCA SSM over dense vegetation periods and regions. Also, it is important to select appropriate evaluation strategies to conduct the SSM and RZSM evaluations according to the situation as the available sites and temporal samplings may bias the evaluation results.

1. Introduction

Surface soil moisture (SSM) and root-zone soil moisture (RZSM) are key state variables in the hydrological cycle and control the exchange of water and energy between land and atmosphere interactions (Peng et al., 2021; Seneviratne et al., 2010). Temporally and spatially continuous soil moisture datasets are beneficial for numerous applications such as climate monitoring (Hirschi et al., 2010; Miralles et al., 2013), applied hydrology (Jackson et al., 2009), evaporation estimation (Martens et al., 2017), drought warning (Chatterjee et al., 2022; Watson et al., 2022), and water resources management (Zhao et al., 2020), especially as agriculture is the primary user of water.

In situ measurements can provide accurate SSM and RZSM information but are insufficient for monitoring large spatiotemporal climate and environmental changes due to the limitations (very time-consuming) of deploying dense networks (Bi et al., 2016; Ochsner et al., 2013). Microwave remote sensing is an effective global SSM monitoring approach owing to its immunity to bad weather and nighttime and the benefit of frequent revisits (Owe et al., 2008). The Advanced Microwave Scanning Radiometer-Earth Observing System/2 (AMSR-E/2) (Koike et al., 2004), Soil Moisture and Ocean Salinity (SMOS) (Kerr et al., 2010), Soil Moisture Active Passive (SMAP) (Entekhabi et al., 2010), and Advanced Scatterometer (ASCAT) (Wagner et al., 2013) are widely known satellites/sensors for providing spatio-temporal SSM information. In addition, a combined SSM product from the European Space Agency Climate Change Initiative (ESA CCI) (Dorigo et al., 2017) benefits from regular updates to improve its quality. RZSM products mostly come currently from land surface model (LSM) outputs, including the enhanced global dataset for the land component of the fifth generation of European (ERA5-Land) (Muñoz-Sabater et al., 2021), the Global Land Data Assimilation System (GLDAS-Noah) (Rodell et al., 2004), *etc.*, due to the constraint on microwave penetration depth (Reichle et al., 2007).

Note that some uncertainties could exist in retrieving SSM in the croplands as vegetation development affects the radiative transfer mechanisms, and irrigation events could affect its spatial distribution (Fan et al., 2015). Previous studies have also reported that the performance of the SSM products in China could be affected by radio-frequency interference (RFI), which corresponds to unwanted man-made emissions received by the satellite sensors, especially at L-band (Al-Yaari et al., 2019; Wigneron et al., 2021; Zhao et al., 2015). In particular, their performance seems to be highly impacted by radio-frequency interference (RFI) in Jiangsu province, mainly for the SMOS L-band radiometer (http://www.grss-ieee.org/rfi_observations.html). Thus, evaluating remotely-sensed and model-based SSM and RZSM data over croplands is essential for their practical applications and further improvements.

Rare investigations have been carried out over the croplands of Jiangsu Province. Until now, most evaluation studies have been conducted either over the whole country (Chen and Yuan, 2020; Jia et al., 2015; Ling et al., 2021; Sun et al., 2017) or in sub-regions (North China Plain (Wang et al., 2016), Central and Eastern Agricultural Area (Yang et al., 2021b), Southwestern China (Peng et al., 2015), Central Tibetan Plateau (Chen et al., 2013; Xing et al., 2021), and Mongolian Plateau (Luo et al., 2020), *etc.*) or specific watersheds (Heihe River (Wang et al., 2021), Luan River (Zheng et al., 2022)) of the Chinese mainland. This can be attributed to the scarcity of *in situ* sites within Jiangsu province that prevent sound evaluations.

Jiangsu, covering an area of 10.26×10^4 km^2, is one of China's most important agricultural provinces. Croplands covered about 60% of the Jiangsu Province. Winter wheat is the second major cereal crop accounting for approximately 30% of the total grain production in China. Thus, the accuracy of the soil moisture datasets is key to the agricultural water management of Jiangsu province (Xu et al., 2018). An *in situ* network including ninety-one sites, deployed by the Jiangsu Meteorological Information Center, provides an opportunity to assess the remotely sensed and model-based soil moisture datasets for croplands in Jiangsu province. This valuable dataset is totally independent of the soil moisture datasets, as these observations are not included in their calibration.

Besides, different evaluation strategies may lead to very different results, which have not been comprehensively considered in previous studies, and thus deserve to be investigated further. Evaluating the SSM and RZSM products from various evaluation strategies could help investigate the impact of these approaches on evaluation results and obtain a relatively fair and comprehensive evaluation. For example, the evaluations can be conducted: i) using all available *in situ* sites and time samplings for each SSM and RZSM product, ii) using all available time samplings of common sites or, iii) using overlapped dates within common sites.

In addition, direct comparison against *in situ* measurements from sparsely distributed networks may not be sufficient for a sound assessment, the results of which could be hindered by the sites' representativeness errors (Xing et al., 2021). The triple collocation analysis (TCA) is another tool that can be implemented at a footprint/pixel scale. TCA was first used in oceanography and then introduced to evaluate the SSM products, as it does not require high-quality reference data and can be used to estimate the error variance of three independent SSM products (Chen et al., 2018a; Dong and Crow, 2017; Kim et al., 2020). Besides, agricultural applications of SSM information require accurate SSM accuracy estimates during the critical crop development period except for the time-invariant SSM accuracy for the whole research period (Wu et al., 2021a). Thus, considering both time-invariant and time-variant TCA-*R* are necessary for accurate SSM retrievals at different time scales, as the latter provides daily accuracy estimates with time (Su et al., 2014).

This study focuses on the Jiangsu province using *in situ* measurements to (i) assess the accuracy of the thirteen SSM products and four RZSM products; (ii) analyze products' performance under different evaluation strategies; (iii) investigate the potential impact factors on the performance of all soil moisture products used in the study.

2. Datasets

2.1. In situ measurements

Ninety-one sites mainly distributed in croplands of Jiangsu province were used for the evaluation (Fig. 1 and Table S1). At each site, the sensors were installed in a horizontal orientation at the topsoil layer (*i.e.*, 0–10 cm), and at other depths from 10 to 100 cm with an interval of 10 cm (Chen et al., 2018b). Each site can simultaneously provide

measurements of volumetric soil moisture content, relative soil humidity, soil weight moisture content, and available soil water storage at a 1-h time interval per day. Data was collected by the Jiangsu Meteorological Information Center and only the *in situ* measurements from January 2011 to December 2018 were available due to the *in situ* measurements in Jiangsu province are not publicly available, and observations after quality controls were retained only. With a flat average elevation of 54 m, Jiangsu province has fourteen different land surface types, of which four types dominate: croplands, savannas, urban areas, and water bodies.

2.2. Satellite and reanalysis SSM and RZSM datasets

Thirteen SSM datasets and three RZSM datasets were collected in this study, including 1) the SMOS-IC version 2 ascending (6:00 a.m.) and descending (6:00 p.m.) SSM product (Li et al., 2020; Wigneron et al., 2021), 2) the AMSR2 LPRM Level 3 X-band (10.7 GHz) descending (1:30 a.m.) and ascending (1:30 p.m.) SSM product (Njoku et al., 2005), 3) the H115-Metop ASCAT ascending (9:30 p.m.) and descending (9:30 a.m.) SSM product (Wagner et al., 2013), 4) the ESA CCI combined, passive and active (hereafter ESA CCI, ESA CCI-P, ESA CCI-A) SSM product (Dorigo et al., 2017), 5) the SMAP-L3 version 8 (Chan et al., 2016), MTDCA version 5 (Konings et al., 2017), SMAP-MCCA version 1 (Zhao et al., 2021) and SMAP-IB version1 (Li et al., 2022) descending (6:00 a.m.) and the SMAP-MCCA version 1 ascending (6:00 p.m.) SSM products, 6) the SMAP-L4, ERA5-Land and GLDAS-Noah SSM (~0–5 cm for SMAP-L4, 0–7 cm for ERA5-Land and 0–10 cm for GLDAS-Noah) and RZSM (0–100 cm) datasets at 0:00 and 12:00 UTC (Muñoz-Sabater et al., 2021; Reichle et al., 2017; Rodell et al., 2004). For more details refer to Table 1 and Supplementary Text.

The retrievals considered "good" in these products are usually used only (Gruber et al., 2020). The quality flags for the above products used

Table 1
Overview of the SSM and RZSM datasets used in this study.

	Datasets	Version	Spatial resolution	Temporal resolution	Product
Satellite products	AMSR2 LPRM	V001	0.25°	Daily	SSM
	SMOS-IC	V2	25 km	Daily	SSM
	SMAP-L3	V8	36 km	Daily	SSM
	SMAP-IB	V1	36 km	Daily	SSM
	MTDCA	V5	9 km	Daily	SSM
	SMAP-MCCA	V1	36 km	Daily	SSM
	ASCAT	H115	12.5 km	Daily	SSM
	ESA CCI Combined/ Passive/ Active	V6.1	0.25°	Daily	SSM
	SMAP-L4	V6	9 km	Daily	SSM and RZSM
Reanalysis products	ERA5-land	V2	0.1°	Hourly	SSM and RZSM
	GLDAS-Noah	V2.1	0.25°	3-Hourly	SSM and RZSM

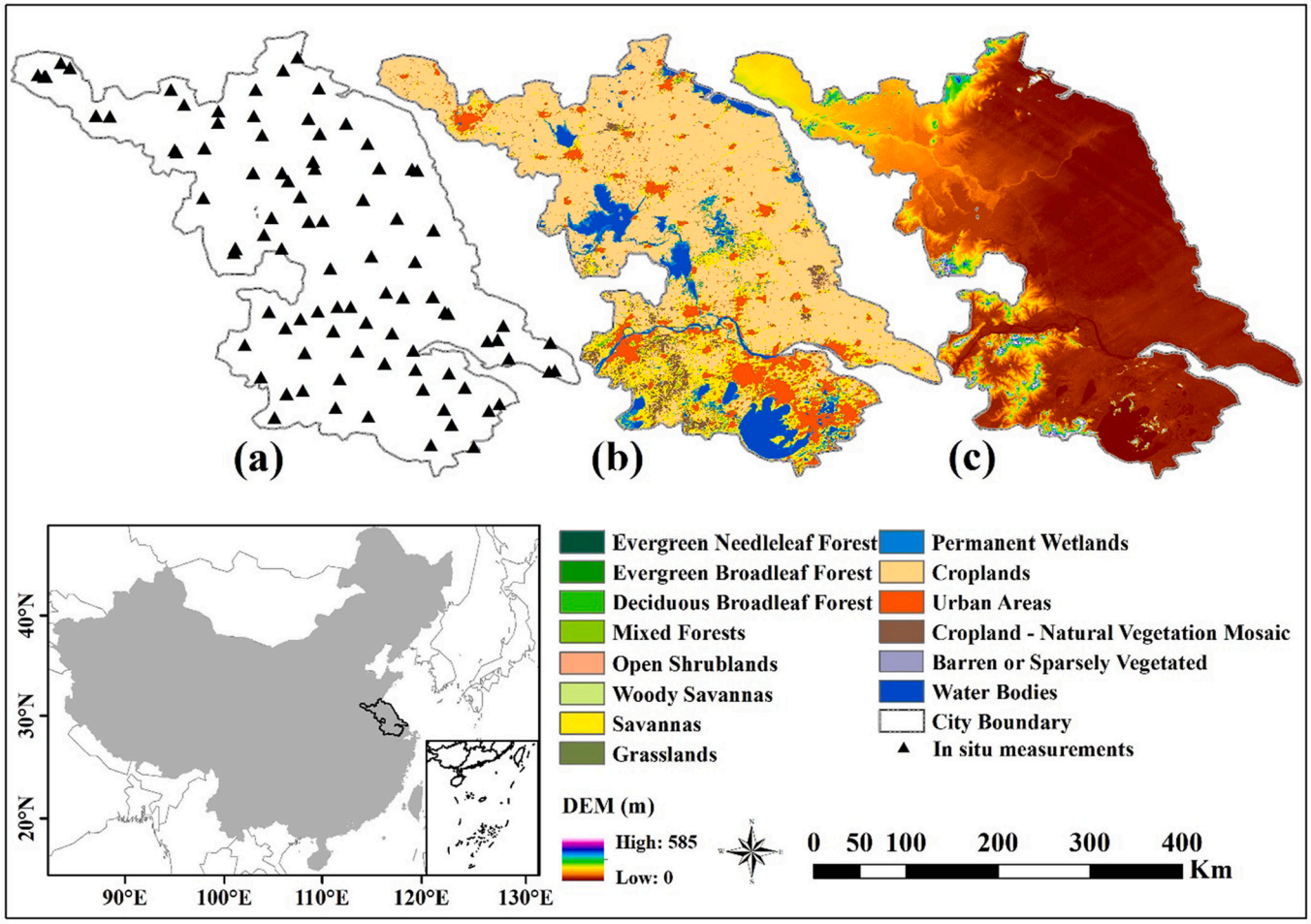

Fig. 1. Overview of the study area. (a) Locations of the *in situ* sites (black triangle). (b) MODIS International Geosphere-Biosphere Programme (IGBP) land cover maps. (c) Altitude above mean sea level in meters with a spatial resolution of 90 m shared freely by the Shuttle Radar Topography Mission (SRTM) (http://srtm.csi.cgiar.org/srtmdata/).

in the study are as follows: 1) AMSR2 LPRM SSM pixels were retained when "snow mass = 0" and "soil temperature > 0 °C"; 2) SMOS-IC SSM pixels were filtered when "Scene flag > 1" and "TB-RMSE > 8 K"; 3) ASCAT SSM pixels were retained when "Frozen or Snow cover probability < 50%" and "Flag = 1"; 4) ESA CCI SSM pixels were retained when "Flag = 0"; 5) SMAP-L3 and MTDCA SSM pixels were only kept when the retrieval quality is recommended. Namely, pixels with open "water fraction > 0.1", "precipitation > 1 mm/h", snow, frozen ground and strong topography were masked. 6) SMAP-IB SSM pixels were filtered when "Scene flag >1"; 6) SMAP-L4, ERA5-Land and GLDAS-Noah SSM and RZSM grids were retained when "snow mass = 0" and "soil temperature > 0 °C" (estimated from GLDAS-Noah).

2.3. Auxiliary datasets

Some auxiliary datasets used to explore the uncertainties of the SSM products are as follows (Table 2): 1) the descending SMAP-L3 L-band VOD product used in the dual-channel algorithm (DCA) retrieval, which is used to characterize the vegetation density; 2) the MODIS IGBP land cover map, which is used to calculate WF to characterize the open water bodies' effect, respectively; 3) the ascending SMOS-IC L-band TB-RMSE data, which is used to represent RFI to characterize the influence of the unwanted man-made emissions received by the L-band satellites (Wigneron et al., 2021). The daily average ERA5-Land precipitation was also collected.

3. Methodology

3.1. Data pre-processing

To quantify a fair inter-comparison, the assessment was carried out for all datasets for the same period (from March 2015 to December 2018). The overpass/output time of each satellite/reanalysis product was matched with the observed time of *in situ* measurements in less than an hour. The product data were then obtained from the pixels/grids corresponding to each site following the nearest grid method (Al-Yaari et al., 2019). Besides, we took multiple *in situ* sites within a satellite/reanalysis grid cell as independent sites and compared them separately, as each site could be partly representative of the grid cell truth values following Xu et al. (2021). Correlation coefficient (*R*) and ubRMSE were used as the major criteria for the assessment, as they are less affected by the depth difference between sites and satellite and reanalysis products (Yang et al., 2020). The metrics were only calculated for the sites with significant correlation coefficients (*P-Value* < 0.05) so that the number of available sites used in the error metrics calculation may vary from one product to the other. The influence of different temporal sampling and available sites on the performance of all products will be discussed later using different evaluation strategies.

3.2. Calculation of RZSM

A depth-weighted mean method was applied to obtain *in situ* RZSM (*i.e.*, the 0–100 cm soil layer) (Gao et al., 2017). The calculation was as follows:

$$\theta_{RZSM} = \frac{2\theta_1 L_1 + (\theta_1 + \theta_2)L_2 + (\theta_2 + \theta_3)L_3 + \ldots + (\theta_{i-1} + \theta_i)L_i}{2(L_1 + L_2 + L_3 + \ldots + L_i)} \quad (1)$$

Where θ_{RZSM} denotes RZSM, θi denotes soil moisture values at the i^{th} layer, and *Li* denotes the i^{th} layer depth, including eight specific depths (*i.e.*, 0–10, 10–20, 20–30, 30–40, 40–50, 50–60, 60–80, 80–100 cm).

The RZSM product was provided by SMAP-L4 and GLDAS-Noah directly. ERA5-Land RZSM could be obtained using a weighted average method by combining the soil moisture values at the first (θ_{7cm}), second (θ_{28cm}), and third (θ_{100cm})) layers (González-Zamora et al., 2016):

$$\theta_{RZSM} = 0.07*\theta_{7cm} + 0.21*\theta_{28cm} + 0.72*\theta_{100cm} \quad (2)$$

The exponential filter proposed by Wagner et al. (1999) and later reformulated in a recursive form by Albergel et al. (2008) was extensively used to retrieve RZSM from satellite SSM products (Cho et al., 2015; Fan et al., 2018). The method assumes a constant pseudo-diffusivity factor that propagates fluctuations in SSM in the attenuated form to RZSM (Rossini and Patrignani, 2021). The recursive formulation to retrieve RZSM from SSM can be written as:

$$SWI_n = SWI_{n-1} + K_n(ms(t_n) - SWI_{n-1}) \quad (3)$$

Where *SWIn* (ranges from 0 to 1) is defined as the soil water index representing the degree of saturation of the RZSM at time t_n. *SWIn* can be translated from relative (%) to absolute volumetric unit (m^3/m^3) by multiplying soil porosity information (Wagner et al., 2013). $ms(t_n)$ is the satellite SSM at time t_n, scaled by the maximum and minimum values during the entire research period. The gain *K* at time t_n can be written as:

$$K_n = \frac{K_{n-1}}{K_{n-1} + e^{-\frac{t_n - t_{n-1}}{T}}} \quad (4)$$

where $t_n - t_{n-1}$ is the difference in days between SSM observations. T represents the infiltration time in days and the only unknown of the function, which is often assumed to be related to soil texture and bulk density (Albergel et al., 2008). The optimal T parameter (T_{opt}) was determined by maximizing the correlation coefficients between the retrieved RZSM and *in situ* RZSM, in which the retrieved RZSM was computed using different T (1–60 days) (Wang et al., 2017). The filter was initialized with SWI1 = ms(t1) and K1 = 1. Since the *in situ* soil porosity information is hard to obtain, the soil porosity values for each site derived from the static information for the ASCAT product obtained from the Harmonized World Soil Database (HWSD) were used (Wagner et al., 2013). The average soil porosity of these sites is 0.54 m^3/m^3 with a standard deviation of 0.03 m^3/m^3. In the study, ESA CCI SSM was coupled with an exponential filter to estimate ESA CCI RZSM for each site in Jiangsu province due to ESA CCI SSM outperformed the other satellite SSM products.

Table 2
Overview of the auxiliary datasets used in this study.

Factors	Database	Spatial resolution	Time period	References
VOD	SMAP-L3 L-band VOD	0.25°	2015–2018	(Chan et al., 2016)
WF	IGBP MODIS land cover	500 m	2015	(Friedl and Sulla-Menashe, 2019)
RFI	SMOS-IC TB-RMSE	25 km	2015–2018	(Wigneron et al., 2021)
Precipitation	ERA5-Land	0.1°	2015–2018	(Muñoz-Sabater et al., 2021)

3.3. Evaluation metrics

3.3.1. In situ-based metrics

Taylor diagram (Taylor, 2001) was used to assess the products' accuracy. Normalized standard deviation (SDV, Eq. (5)) indicates the ratio between the evaluated products (*i.e.*, θ_{EST}) and referenced datasets (*i.e.*, θ_{REF}) standard deviations (Cho et al., 2017; Kim et al., 2018). *R* (Eq. (6)) and cRMSE (Eq. (7)) are the Pearson correlation coefficient and the centered Root Mean Square Error between θ_{EST} and θ_{REF}, respectively.

$$SDV = \frac{\sqrt{\overline{(\theta_{EST} - \overline{\theta_{EST}})^2}}}{\sqrt{\overline{(\theta_{REF} - \overline{\theta_{REF}})^2}}} \quad (5)$$

$$R = \sqrt{1 - \frac{\overline{(\theta_{EST} - \theta_{REF})^2}}{\overline{(\theta_{EST} - \overline{\theta_{REF}})^2}}} \quad (6)$$

$$cRMSE = \sqrt{\overline{[(\theta_{EST} - \overline{\theta_{EST}}) - (\theta_{REF} - \overline{\theta_{REF}})]^2}} \quad (7)$$

where θ_{EST} is either the evaluated SSM or RZSM product; θ_{REF} is the *in situ* SSM or RZSM; the overbar indicates the temporal mean operator (*i.e.*, $\overline{\theta_{EST}}$ and $\overline{\theta_{REF}}$).

In addition, three commonly used statistical indicators, namely averaged bias (Bias, Eq. (8)), Slope (Eq. (9)) and RMSE (Eq. (10)), was also applied to examine the accuracy of these datasets (Entekhabi et al., 2010). Since the RMSE (Eq. (10)) could be compromised when biases exist between *in situ* measurements and satellite and model-based pixels/grids (Al-Yaari et al., 2016), the ubRMSE (Eq. (11)) is often optimal to evaluate soil moisture products (Yang et al., 2020).

$$Bias = \overline{\theta_{EST} - \theta_{REF}} \quad (8)$$

$$Slope = \frac{[(\theta_{REF} - \overline{\theta_{REF}})(\theta_{EST} - \overline{\theta_{EST}})]}{(\theta_{REF} - \overline{\theta_{REF}})^2} \quad (9)$$

$$RMSE = \sqrt{\overline{(\theta_{EST} - \theta_{REF})^2}} \quad (10)$$

$$ubRMSE = \sqrt{RMSE^2 - Bias^2} \quad (11)$$

Considering the limited available sites with significant ($P\text{-}Value < 0.05$) correlation coefficients and low temporal sampling of and SMOS-IC SSM due to the L-band RFI issue in China (Al-Yaari et al., 2019; Wigneron et al., 2021), the SSM products were evaluated against *in situ* measurements following four cases (the used SSM products for each case can be seen in Table 3):

Case 1. All available sites with significant correlation coefficients for each product were used. The number of sites for the ESA CCI, SMOS-IC, ASCAT, LPRM, MTDCA, SMAP-L3, SMAP-L4, SMAP-MCCA, SMAP-IB, ERA5-Land, and GLDAS-Noah products is 52, 79, 69, 69, 90, 89, 33, 43, 59, 56, 88, 70 and 27, respectively.

Case 2. The common sites with significant correlation coefficients for all products were used. The number of available sites for the six products is 6.

Case 3. The common sites with significant correlation coefficients for all products except SMOS-IC and SMAP-IB were used. SMOS-IC is available for a limited data number compared to the other products and was therefore excluded in this case. There are 19 sites available for the other eleven products.

Case 4. The overlapped dates within common sites in Case 3 (*i.e.*, days where all satellite and model-based SSM observations are available) for all products except SMOS-IC and SMAP-IB were used. There are 3 sites available for the other eleven products.

Table 3
List of the used SSM and RZSM products for each case.

Cases	SSM	RZSM
Case1	ASCAT, ESA CCI, ESA CCI-P, ESA CCI-A, SMOS-IC, LPRM, MTDCA, SMAP-L3, SMAP-L4, SMAP-MCCA, SMAP-IB, ERA5-Land, GLDAS-Noah	ESA CCI RZSM, SMAP-L4, ERA5-Land, GLDAS-Noah
Case2	ASCAT, ESA CCI, ESA CCI-P, ESA CCI-A, SMOS-IC, LPRM, MTDCA, SMAP-L3, SMAP-L4, SMAP-MCCA, SMAP-IB, ERA5-Land, GLDAS-Noah	ESA CCI RZSM, SMAP-L4, ERA5-Land, GLDAS-Noah
Case3	ASCAT, ESA CCI, ESA CCI-P, ESA CCI-A, LPRM, MTDCA, SMAP-L3, SMAP-L4, SMAP-MCCA, ERA5-Land, GLDAS-Noah	ESA CCI RZSM, SMAP-L4, ERA5-Land, GLDAS-Noah
Case4	ASCAT, ESA CCI, ESA CCI-P, ESA CCI-A, LPRM, MTDCA, SMAP-L3, SMAP-L4, SMAP-MCCA, ERA5-Land, GLDAS-Noah	

For RZSM, three cases were considered (the RZSM datasets for each case can be seen in Table 3):

Case 1. All available sites with significant correlation coefficients for each product were used. The number of sites for the ESA CCI, ERA5-Land, GLDAS-Noah and SMAP-L4 products is 78, 83, 77 and 85, respectively.

Case 2. The common sites with significant correlation coefficients for all products were used. The number of available sites for the four products is 75.

Case 3. The overlapped dates (*i.e.*, days where all RZSM observations are available) for all products were used. There are 73 sites available for the four products.

Case1 for SSM and RZSM is used assuming that the final users may use these products separately (Al-Yaari et al., 2019), and hence limiting the evaluation to common dates may not correspond to the actual accuracy that the end-user will obtain. Cases 2 and 3 for SSM and Case 2 for RZSM are used to evaluate the influence of the available sites on our evaluation results, and Case 4 for SSM and Case 3 for RZSM are used to evaluate the influence of time series length and data sampling in the comparisons.

3.3.2. TCA-based metrics

In addition to *in situ* measurements, TCA, an approach commonly used in the quality assessment of SSM products (Dong and Crow, 2017), was also applied to provide a complimentary evaluation of the SSM quality in Jiangsu province. Prior to performing the TCA, we reserved the anomaly SSM data by removing the climatology of each SSM product, as its climatology can be correlated and thus cause the TCA-based numbers to be over-graded (Dong et al., 2020a; Draper et al., 2013; Kim et al., 2020). The anomaly SSM data was calculated as follows:

$$\theta_{anom}(t) = \frac{\theta_t - \overline{\theta_{(t-17:t+17)}}}{SD\left(\theta_{(t-17:t+17)}\right)} \quad (12)$$

where $\theta_{anom}(t)$ is the SSM value at day (t) and $\overline{\theta_{(t-17:t+17)}}$ and $SD(\theta_{(t-17:t+17)})$ are the mean and standard deviation over a sliding window of 35 days, respectively (Albergel et al., 2012; Gruber et al., 2020).

Since the TCA is based on the strong assumption of independent errors for the three SSM inputs (*i.e.*, three collocated SSM products) (Gruber et al., 2016), a conventional combination of SSM triplets comprising passive/active microwave product and a model-based product was applied. If a product is combined or assimilated into another system, the two data sets should not be considered together (Kim et al., 2020). For example, the ESA CCI combined SSM products was not considered in TCA implementations. In addition, the triplets composing of both ASCAT and ERA5-Land were removed in the updated version, due to that the ASCAT SSM data was assimilated into ERA5. Also, the triplets composing of both ESA CCI and GLDAS-Noah were removed due to that the GLDAS-Noah was used in the retrievals of ESA CCI. SMOS-IC was not used here due to very limited available data. Thus, from the thirteen SSM products, five triplets were considered possible for each product (Table 4). Considering the skill estimates for some SSM products could be obtained from more than one triplet, we averaged all skill estimates for each product for increased precious

Table 4
List of the possible triplets used in the TCA implementations.

Triplets	Passive	Active	Model
1	LPRM	ASCAT	GLDAS-Noah
2	SMAP-L3		
3	MTDCA		
4	SMAP-MCCA		
5	SMAP-IB		

(Gruber et al., 2020; Zheng et al., 2022). Here, we focused on the TCA-based R (hereafter TCA-R), as follows:

$$R_x = \sqrt{\frac{\sigma_{xy}\sigma_{xz}}{\sigma_{xx}\sigma_{yz}}} \tag{13}$$

where x, y, and z refer to the SSM triplets and σ is the covariance between collocated SSM products. The TCA-R indicates the linear correlation against the unknown truth (Gruber et al., 2020; McColl et al., 2014). To ensure the reliability of the metrics, the TCA was only performed for SSM triplets with at least 100 samples (Kim et al., 2020).

Here, both time-invariant and time-variant TCA-R were estimated by applying TCA to SSM data in the whole research period and to SSM samples that were collected for every daily time step by considering the same triplets. Following Wu et al. (2021a), we used a 100-day window to estimate time-variant TCA-R to keep sufficient statistical power. The TCA-R was calculated only when the number of triplet samples in the time window was >90. Considering the temporal samples for each triplet within a 100-day window may not be sufficient to meet the

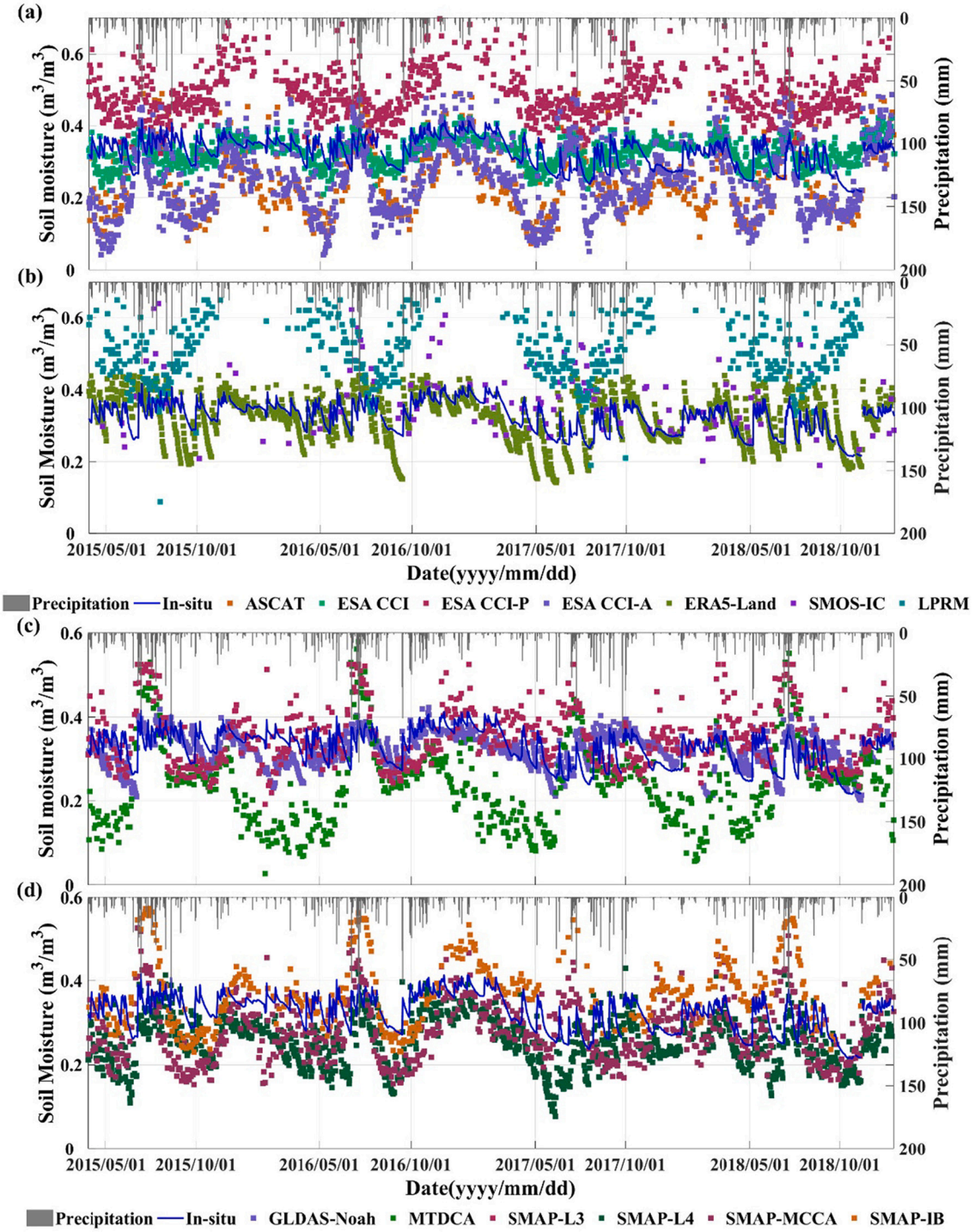

Fig. 2. Time series of the *in situ* SSM and the thirteen SSM products for site M5401 from March 2015 to December 2018 in Jiangsu province for nighttime. Blue solid lines represent *in situ* measurements at 6:00 a.m. Averaged daily precipitation is represented by grey vertical bars. (For interpretation of the references to colour in this figure legend, the reader is referred to the web version of this article.)

sample number requirement (> 90) in our time-variant TCA implementation, a linear interpolation within a 3-day time window was applied to fill the temporal gap existing in the active and passive SSM time series in Table 4. Although the interpolation may introduce extra error into the TCA-*R*, the extra error was assumed to be small enough to be ignored (see Wu et al. (2021a) and Leroux et al. (2013) for more details).

4. Results

Evaluations of the SSM and RZSM products for the nighttime and daytime were made, and the results showed the nighttime SSM and RZSM products had similar performances to the daytime SSM and RZSM products. Thus, the evaluation results for the nighttime products were presented to maintain a simplicity of presentation and interpretation. The evaluation results for daytime products were provided in the Supplementary Text.

4.1. SSM evaluation

4.1.1. In situ-based metrics

The performance criteria presented in Taylor diagrams and four scores were computed between products and *in situ* SSM from March 2015 to December 2018 (Figs. 2, 3, and Table 5) and see Fig. S5 for the performance of the SSM products for the individual *in situ* site. As mentioned before, four cases were carefully considered.

Fig. 2 shows the temporal variations of the thirteen SSM products, the *in situ* SSM and rainfall of one representative site (*i.e.*, site M5401) with relative complete temporal samplings for nighttime. All SSM products except for LPRM and ESA CCI-P correspond well with rainfall, with the SSM increasing during rainfall events and decreasing after rainfall events. The ERA5-Land, SMAP-L4, GLDAS-Noah and ESA CCI SSM products captured well the annual cycle of the *in situ* measurements. In comparison, the other nine SSM products were more scattered than the products mentioned above. ESA CCI-P and LPRM overestimated *in situ* SSM with large wet biases, while ESA CCI-A, ASCAT and MTDCA SSM tended to underestimate *in situ* SSM. Despite the lowest number of retrievals for SMOS-IC due to the effects of RFI in the study area, it could marginally follow the temporal evolution of *in situ* SSM.

Fig. 3(a) shows the overall performance obtained by each product over all available sites (Case 1). Regarding *R*, the ERA5-Land and SMAP-L4 SSM products outperformed the other eleven datasets with a higher *R* of 0.58. It was followed by ESA CCI, ESA CCI-A and GLDAS-Noah (median $R = 0.42$ for ESA CCI and $R = 0.40$ for ESA CCI-A and GLDAS-Noah) (Table 5). LPRM failed to reproduce the temporal evolution of observed SSM with a low *R* and large variability in the SSM retrievals at available sites (median $R = 0.20$ and SD > 0.09). Regarding ubRMSE (Table 5), the ESA CCI and GLDAS-Noah products outperformed the others, with the same lowest ubRMSE of 0.04 m^3/m^3, followed by SMAP-L4 and ERA5-Land with a value of 0.05 m^3/m^3 and 0.06 m^3/m^3, respectively. For the rest datasets, the ubRMSE values all exceeded 0.07 m^3/m^3, and LPRM occupied the highest (median ubRMSE = 0.10 m^3/m^3). Six SSM datasets (*i.e.*, ESA CCI, ESA CCI-P, ERA5-Land, GLDAS-Noah, LPRM, and SMAP-L3) overestimated *in situ* SSM, in which LPRM and ESA CCI-P obtained overall higher bias (median bias = 0.19 m^3/m^3 for LPRM and bias = 0.12 m^3/m^3 for ESA CCI-P) than the other four SSM products

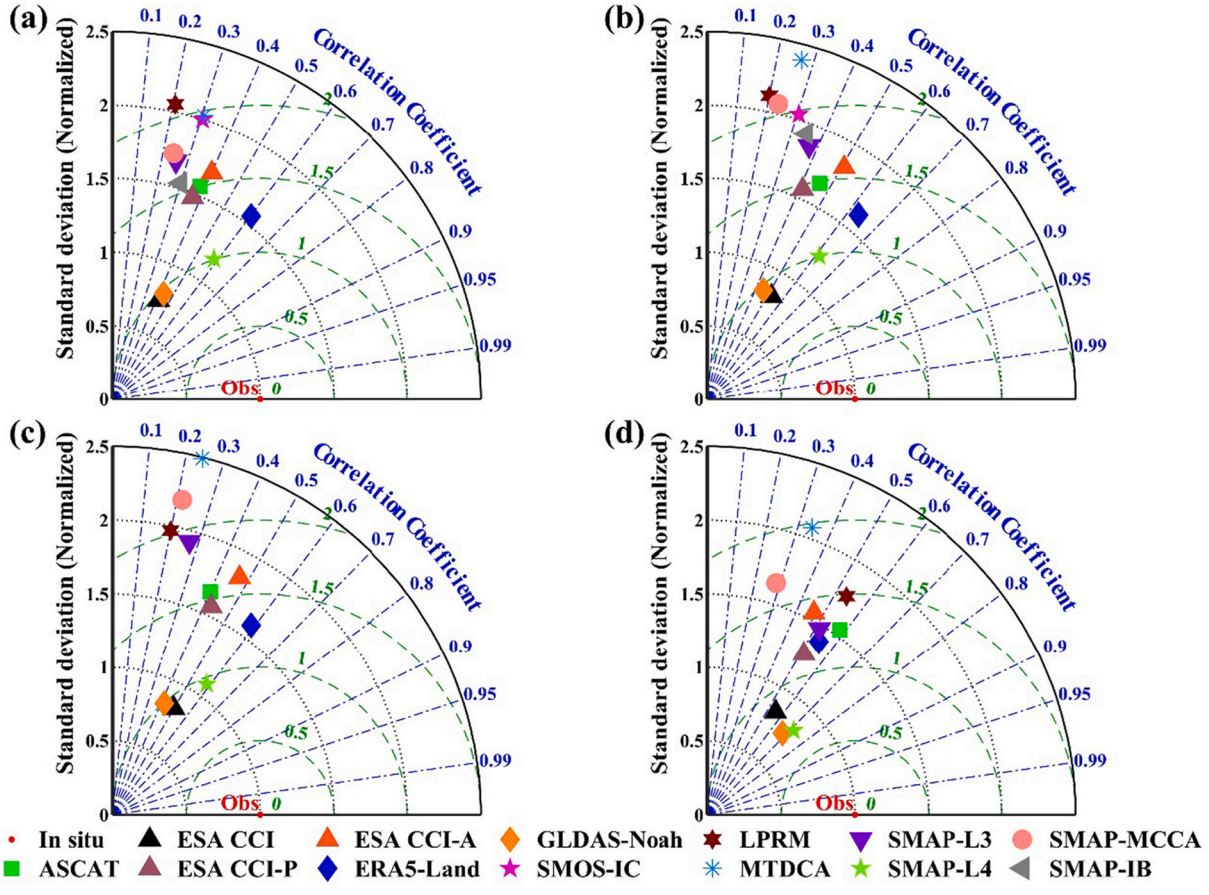

Fig. 3. Taylor's diagrams displaying a statistical comparison between ASCAT, ESA CCI, ESA CCI-P, ESA CCI-A, ERA5-Land, GLDAS-Noah, SMOS-IC, LPRM, MTDCA, SMAP-L3, SMAP-L4, SMAP-MCCA and SMAP-IB SSM products with the *in situ* observed SSM for morning time during 2015–2018. The green dash lines represent the centered RMSE (cRMSE) values, which distance the 'Obs' point. (a) – (d) show the median error metrics from Case 1 to Case 4, respectively. (For interpretation of the references to colour in this figure legend, the reader is referred to the web version of this article.)

Table 5
Summary median metrics of comparing thirteen SSM products with *in situ* measurements for each Case for nighttime. Bias and ubRMSE are both in m^3/m^3. *N* is the average number of samples. The bold font highlights the best results for each error metric.

Cases	Products	bias	ubRMSE	*R*	slope	*N*	Sites	Cases	Products	bias	ubRMSE	*R*	slope	*N*	Sites
Case 1	ASCAT	−0.05	0.07	0.38	0.63	607	52	Case 3	ASCAT	−0.09	0.07	0.40	0.77	612	19
	ESA CCI	0.03	**0.04**	0.42	0.30	1277	79		ESA CCI	**−0.01**	**0.04**	0.52	0.46	1285	19
	ESA CCI-P	0.12	0.07	0.37	0.54	898	69		ESA CCI-P	0.10	0.07	0.43	0.71	996	19
	ESA CCI-A	−0.07	0.07	0.40	0.71	1266	69		ESA CCI-A	−0.09	0.07	0.45	0.88	1276	19
	ERA5-Land	0.02	0.06	**0.58**	**0.88**	1293	90		ERA5-Land	**0.01**	0.06	0.59	**0.89**	1271	19
	GLDAS-Noah	0.02	**0.04**	0.40	0.30	1292	89		GLDAS-Noah	**−0.01**	**0.04**	0.45	0.36	1271	19
	SMOS_IC	−0.04	0.09	0.30	0.63	110	33		SMOS_IC	–	–	–	–	–	–
	LPRM	0.19	0.10	0.20	0.41	632	43		LPRM	0.16	0.09	0.20	0.44	672	19
	MTDCA	−0.09	0.09	0.29	0.63	636	59		MTDCA	−0.10	0.11	0.27	0.67	644	19
	SMAP_L3	**0.01**	0.08	0.26	0.46	602	56		SMAP_L3	−0.04	0.08	0.31	0.54	596	19
	SMAP_L4	−0.06	0.05	**0.58**	0.68	1293	88		SMAP_L4	−0.10	0.05	**0.60**	0.69	1271	19
	SMAP_MCCA	−0.02	0.08	0.24	0.45	626	70		SMAP_MCCA	−0.07	0.10	0.21	0.46	593	19
	SMAP_IB	−0.02	0.07	0.30	0.42	212	27		SMAP_IB	–	–	–	–	–	–
Case 2	ASCAT	−0.10	0.07	0.45	0.86	623	6	Case 4	ASCAT	−0.06	0.05	0.58	**0.94**	88	3
	ESA CCI	−0.02	**0.04**	0.53	0.42	1270	6		ESA CCI	−0.04	0.04	0.55	0.44	88	3
	ESA CCI-P	0.08	0.06	0.43	0.78	1032	6		ESA CCI-P	0.06	0.05	0.51	0.61	88	3
	ESA CCI-A	−0.10	0.07	0.50	**0.98**	1275	6		ESA CCI-A	−0.06	0.05	0.47	0.80	88	3
	ERA5-Land	**0.01**	0.06	**0.61**	0.90	1276	6		ERA5-Land	**0.00**	**0.02**	0.54	0.90	88	3
	GLDAS-Noah	**−0.01**	**0.04**	0.45	0.37	1276	6		GLDAS-Noah	−0.03	0.03	0.68	0.52	88	3
	SMOS_IC	−0.12	0.10	0.30	0.71	138	6		SMOS_IC	–	–	–	–	–	–
	LPRM	0.15	0.11	0.20	0.47	762	6		LPRM	0.14	0.13	0.54	0.84	88	3
	MTDCA	−0.09	0.11	0.24	0.73	656	6		MTDCA	−0.06	**0.02**	0.34	0.70	88	3
	SMAP_L3	−0.05	0.09	0.37	0.63	602	6		SMAP_L3	−0.06	0.03	0.52	0.70	88	3
	SMAP_L4	−0.13	0.05	0.60	0.88	1276	6		SMAP_L4	−0.10	0.10	**0.72**	0.84	88	3
	SMAP_MCCA	−0.08	0.10	0.21	0.56	597	6		SMAP_MCCA	−0.07	0.04	0.28	0.42	88	3
	SMAP_IB	−0.04	0.10	0.33	0.69	177	6		SMAP_IB	–	–	–	–	–	–

(median bias <0.03 m^3/m^3). In contrast, ESA CCI-A, SMAP-L4 and ASCAT got large systematical dry biases against *in situ* SSM (median bias < −0.05 m^3/m^3).

Fig. 3(b) shows the overall performance on common sites for all products (Case 2), which was almost the same as the performance of all available sites for each product above. ERA5-Land and SMAP-L4 outperformed the others, with a higher *R* of 0.61 and 0.60, respectively. It was followed by ESA CCI, ESA CCI-A, GLDAS-Noah, ASCAT and ESA CCI-P (median $R > 0.43$). Similar to Case1, ESA CCI and GLDAS-Noah obtained the lowest ubRMSE (median ubRMSE = 0.04 m^3/m^3), while LPRM had the poorest performance in Case 2 with the lowest *R* of 0.2 and the highest ubRMSE and wet bias (median ubRMSE = 0.11 m^3/m^3 and bias = 0.15 m^3/m^3).

Fig. 3(c) shows the overall performance for all products except SMOS-IC and SMAP-IB over common sites (Case 3). With regard to *R*, SMAP-L4 and ERA5-Land outperformed the others, with a higher *R* of 0.60 and 0.59. It was followed by ESA CCI with *R* of 0.52. Regarding errors, the ESA CCI and GLDAS-Noah products obtained the best estimates comparing the rest, with the lowest ubRMSE (median ubRMSE = 0.04 m^3/m^3) and bias (median bias = −0.01 m^3/m^3), respectively, followed by ERA5-Land (median ubRMSE = 0.06 m^3/m^3 and bias = 0.01 m^3/m^3).

Fig. 3(d) shows the overall performance on common dates for all products except SMOS-IC and SMAP-IB (Case 4). SMAP-L4 performed better than the other SSM products, with the highest *R* (median *R* = 0.72). It was followed by GLDAS-Noah, ASCAT, ESA CCI, EREA5-Land, LPRM (median $R > 0.54$). Nevertheless, the largest errors were also obtained by LPRM with the highest bias (0.14 m^3/m^3) and ubRMSE (0.13 m^3/m^3). The good ability in capturing the SSM temporal variation was reconfirmed by the slope obtained between ERA5-Land and observed SSM with a value of 0.90, which is very close to 1. In addition, ERA5-Land had the lowest bias with a negligible value (close to zero) and ubRMSE (0.02 m^3/m^3). It was followed by GLDAS-Noah and ESA CCI (bias = −0.03 m^3/m^3 and bias = −0.04 m^3/m^3).

Overall, the model-based and combined SSM products (*i.e.*, ERA5-Land, SMAP-L4, ESA CCI/ESA CCI-P/ESA CCI-A, GLDAS-Noah) performed better than the active SSM product (*i.e.*, ASCAT), than the passive satellite SSM products (*i.e.*, SMAP-L3, SMOS-IB, SMAP-IC, MTDCA, SMAP-MCCA and LPRM) in Jiangsu province for all cases except Case4, in which LPRM had better performance than ESA CCI-P and ESA CCI-A when considering *R* values. It was suggested that the number of available *in situ* sites and temporal sampling for the SSM products do influence their performances (note that the available number of SMOS-IC and SMAP-IB SSM retrievals is limited in Jiangsu province in comparison to the other products).

4.1.2. TCA-based metrics

Prior to the time-invariant and time-variant TCA implementation, it is necessary to clarify the impact of the error cross-correlation (ECC) for each SSM triplet comprising a passive/active microwave product and a model-based product. The ECC between passive and active satellite SSM products has been found to have a limited impact on the TCA implementation (Chen et al., 2018a). Here, the TCA-*R* calculated using the SSM anomalies of *in situ*-based triplets (*i.e.*, *in situ*, active, passive) were also considered and compared with those of the model-based triplets in Table 4 to clarify the impact of the ECC between model-based and satellite-based SSM products, as the *in situ* measurements was considered as an independent SSM data. A small ECC impact could be indicated by that model-based TCA-*R* values are consistent with *in situ*-based TCA-*R* and their differences are small (Wu et al., 2021a).

Fig. 4 shows the differences in *R* for GLDAS-Noah-based and *in situ*-based TCA-*R* for both time-invariant TCA and time-variant TCA implementation. It can be seen that the differences between them for all triplets were small as associated median values of the difference in *R* were distributed in the range from −0.19 to 0.14 for time-invariant TCA implementation and from −0.07 and 0.10 for time-variant TCA implementation, respectively. In addition, the scatterplots in Figs. S6 and S7 also show that the majority of the scatter points are distributed near the 1:1 line, indicating that the GLDAS-Noah-based TCA-*R* values were highly consistent with the *in situ*-based TCA-*R*. Based on the aforementioned two reasons, we concluded that the ECC between model-based and satellite-based SSM products can barely impact the TCA implementations. Fig. 5 shows the comparison between the time-invariant and time-variant TCA-*R* and *in situ*-based *R* calculated using the SSM anomalies for seven SSM products. Similar performances were observed between TCA-*R* and *in situ*-based *R*, indicating the robustness of the TCA

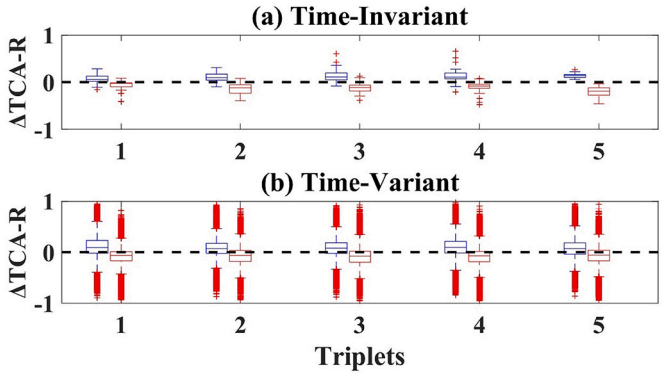

Fig. 4. Boxplots of the differences between triplets 1–5 (in Table 4) and *in situ*-based TCA-*R* calculated using SSM anomalies for both (a) time-invariant and (b) time-variant TCA implementations. The boxplots in blue and red indicate active and passive products, respectively. (For interpretation of the references to colour in this figure legend, the reader is referred to the web version of this article.)

method. Generally, the MTDCA, SMAP-IB, and GLDAS-Noah SSM products performed better than ASCAT, SMAP-L3, SMAP-MCCA and LPRM with higher TCA-*R*. Besides, a combination of SSM triplets comprising *in situ* measurements, GLDAS-Noah and passive/active microwave products was applied to compare the performance of the active *versus* passive SSM products (Fig. S8), and the performances for the passive/active microwave products were almost the same with the results above. In general, the *R* values for all SSM products obtained from both time-invariant and time-variant TCA implementations were higher than *in situ*-based *R*, suggesting that the TCA implementation may statistically correct the random errors of the *in situ* measurements.

In addition, the time-invariant and time-variant TCA-*R* values calculated using the simple SSM anomalies were also presented in the Supplementary Information (Fig. S12) to provide complementary information for readers. Simple SSM anomalies were calculated by removing the climatology from the original SSM time series. Similar TCA-*R* values calculated by the simple SSM anomalies (Fig. S12) and normalized SSM anomalies (Fig. 5) were observed.

4.2. RZSM evaluation

Since ESA CCI outperformed the other satellite SSM products, it was first coupled with an exponential filter to estimate ESA CCI RZSM for each site in Jiangsu province. Then, four RZSM products (*i.e.*, ESA CCI, ERA5-Land, GLDAS-Noah and SMAP-L4 RZSM) were evaluated against the *in situ* measurements by considering three cases and see Fig. S13 for the performance of the RZSM products for the individual *in situ* site. The TCA implementation for RZSM was not conducted as the applied RZSM products could hardly meet the strong assumption of independent errors for the three RZSM inputs.

Fig. 6 presents the correlation coefficients (*R*) values computed between the *in situ* RZSM and ESA CCI RZSM retrievals using different T parameters (1–60 days) with the exponential filter method and the distribution of the number of sites with T_{opt}. Although the T_{opt} varies from one site to another, a relatively higher number of sites was ranged from 7 days to 10 days than the other T values. Besides, it can be seen the optimal median *R* ($R = 0.57$) between *in situ* RZSM and the retrieved RZSM was observed in $T_{opt} = 10$ days. Thus, an overall value of T_{opt} for Jiangsu province was determined to be 10 days. As illustrated over one representative site, the temporal evolution of the ESA CCI RZSM retrievals was well consistent with the *in situ* RZSM, and present lower frequency variations than the ESA CCI SSM (Fig. 7).

Fig. 8 shows the temporal evolution of the four RZSM products along with the *in situ* RZSM for three representative sites (*i.e.*, site 58,235, 58,252 and M5401) from March 2015 to December 2018. It can be seen that these products underestimated but captured well the temporal evolution of the *in situ* RZSM.

For all three cases, the four RZSM products were almost performed the same (Fig. 9 and Table 6). Regarding correlation coefficient (*R*), ESA-CCI, ERA5-Land and SMAP-L4 obtained better scores than GLDAS-Noah, with a higher median $R > 0.54$. The slope of SMAP-L4 was closer to 1 for all cases, relative to GLDAS-Noah, ranging from 0.52 to 0.58. Regarding ubRMSE, all products performed well with low median

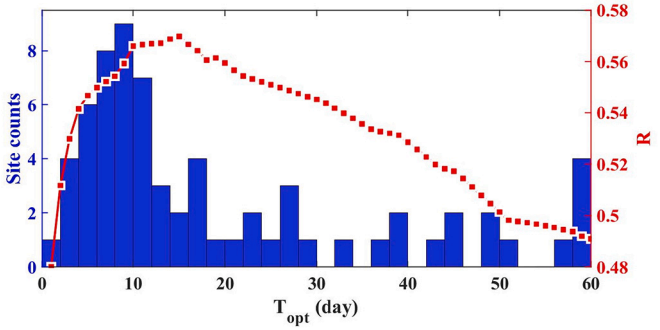

Fig. 6. The distribution of the number of sites for Topt (left y axis) and the median R for all sites with a range of T values (right y axis). The median R was only calculated for the sites with significant correlation coefficients (*P-Value* < 0.05).

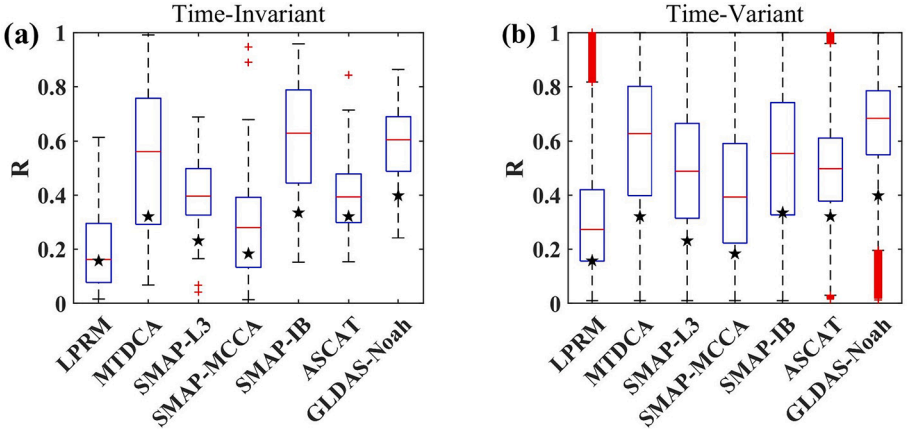

Fig. 5. Boxplots of the (a) time-invariant and (b) time-variant TCA-*R* for LPRM, MTDCA, SMAP-L3, SMAP-MCCA, SMAP-IB, ASCAT and GLDAS-Noah. The black stars indicate the median *R* of *in situ*-based *R* calculated using normalized SSM anomalies.

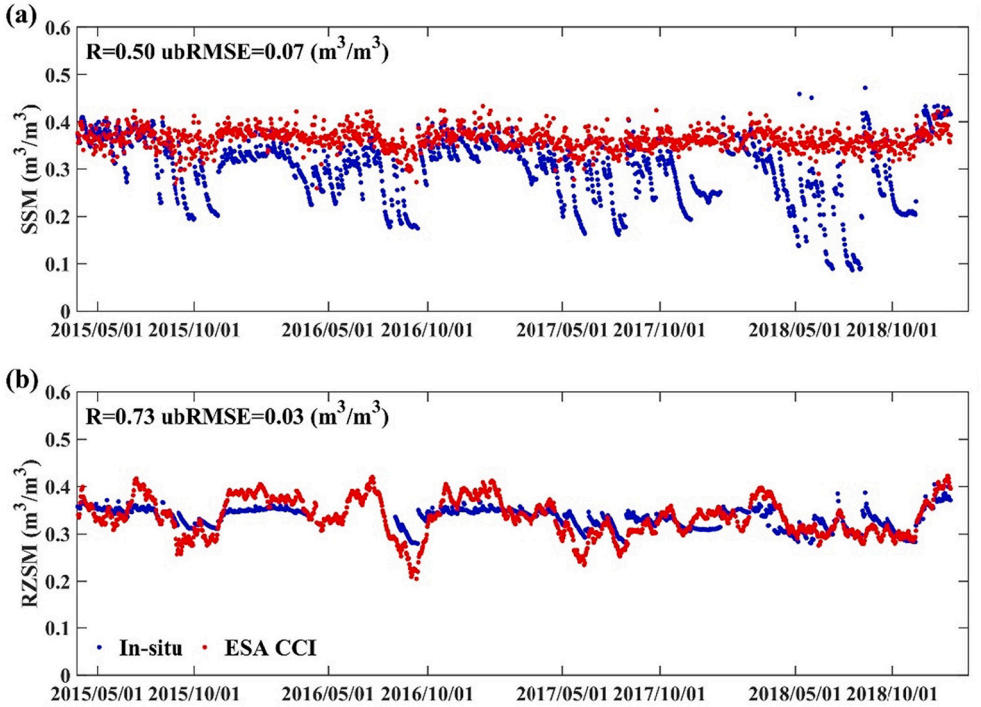

Fig. 7. Time series of (a) *in situ* SSM over the 0–10 cm soil layer and ESA CCI SSM, and (b) *in situ* RZSM over the 0–100 cm soil layer and ESA CCI RZSM at the site 58,252 during 2015–2018.

ubRMSE values (ubRMSE <0.05 m^3/m^3). The RZSM products were mostly dryer than the *in situ* RZSM with median bias ranging from -0.04–-0.08 m^3/m^3.

5. Discussion

The evaluation results showed that the model-based and combined SSM products (*i.e.*, ERA5-Land, SMAP-L4, ESA CCI/ESA CCI-P/ESA CCI-A, GLDAS-Noah) performed better than the other SSM and RZSM products. It could be partly attributed to that the LSM of the model-based products has been substantially updated, leading to better SSM and RZSM dynamics. For instance, a revised soil hydrology parameterization scheme for ERA5-Land (the Carbon Hydrology-Tiled ECMWF Scheme for Surface Ex155 changes over Land: CHTESSEL) was used by introducing an improved soil hydrologic conductivity formulation, diffusivity, and surface runoff based on variable infiltration capacity (Muñoz-Sabater et al., 2021). This result contrasts with our previous SSM and RZSM evaluation, which revealed the poor performance of ERA5-Land over the permafrost regions of the Qinghai-Tibet plateau (Xing et al., 2021). This could be partly explained by the impact of the freezing and thawing cycle in such areas, which does not exist in Jiangsu province, and has not been fully considered within the ERA5-Land LSM (Hu et al., 2020). This result is also in line with Wu et al. (Wu et al., 2021b), reporting that the ERA5-Land SSM products had better performance in southern humid areas than in northern arid and cold regions in China.

5.1. Potential errors for the SSM datasets

The evaluation results showed that the SSM datasets had different performances in Jiangsu province. The accuracy of these datasets could be impacted by many factors, like vegetation, topographic complexity, water bodies, RFI, *etc.* (maps of the relating reference variables like the land cover, DEM and VOD were presented in Figs. 1(b) and (c) and Fig. S14). Here, the correlation coefficients between the accuracy of the thirteen SSM datasets (*i.e.*, correlation coefficients (R) between observations and each SSM product) and the values of the influence factors were calculated to explore the potential influence factors (Table 7). Since the errors for each SSM product were investigated separately, the significant R between the SSM products and the *in situ* measurements calculated by all available sites were used (*i.e.*, Fig. 3(a) and Case 1 in Table 5). The available sites for the ASCAT, ESA CCI, ESA CCI-P, ESA CCI-A, ERA5-Land, GLDAS-Noah, SMOS-IC, LPRM, MTDCA, SMAP-L3, SMAP-L4, SMAP-MCCA and SMAP-IB products in Case 1 are 52, 79, 69, 69, 90, 89, 33, 43, 59, 56, 88, 70 and 27, respectively. In the following section, only the potential factors having a significant (*p-value* < 0.05) correlation with the accuracy of the SSM products were shown and discussed.

5.1.1. Water fraction (WF)

Open water bodies cause substantial uncertainties in the satellite-derived and model-based SSM retrievals (Yang et al., 2021a). The pixels or grids contaminated by coastal areas or inland water bodies physically lead to low TB, backscatters, and temperatures for passive, and active satellite sensors and models, respectively, resulting in increasing/decreasing values of SSM retrievals accordingly (Gouweleeuw et al., 2012; Paulik et al., 2014).

Fig. S15 and Table 7 showed that the accuracy of the ERA5-Land and GLDAS-Noah SSM products were significantly negatively correlated with WF with R of -0.43 and -0.26, suggesting the higher accuracy of the two SSM products over the sites having low WF. Besides, the biases of the thirteen SSM products for different WFs were also displayed in Fig. 10, it can be seen that ERA5-Land and GLDAS-Noah exhibited wet biases over the sites with high WF. For example, the median bias for GLDAS-Noah SSM was approximately 0.02 m^3/m^3 when WF ranges from 0 to 0.1, approximately 0.04 m^3/m^3 when WF ranges from 0.1 to 0.3 and reached 0.09 m^3/m^3 when WF ranges from 0.3 to 0.5 (Fig. 10). This is in line with the result of Li et al. (2012), which found that the grids associated with high WF lead to low temperatures and thus less water evaporation, leading to an increase in SSM.

In addition, a similar increasing pattern of the SSM bias with the increase of WF was founded between ESA CCI and GLDAS-Noah,

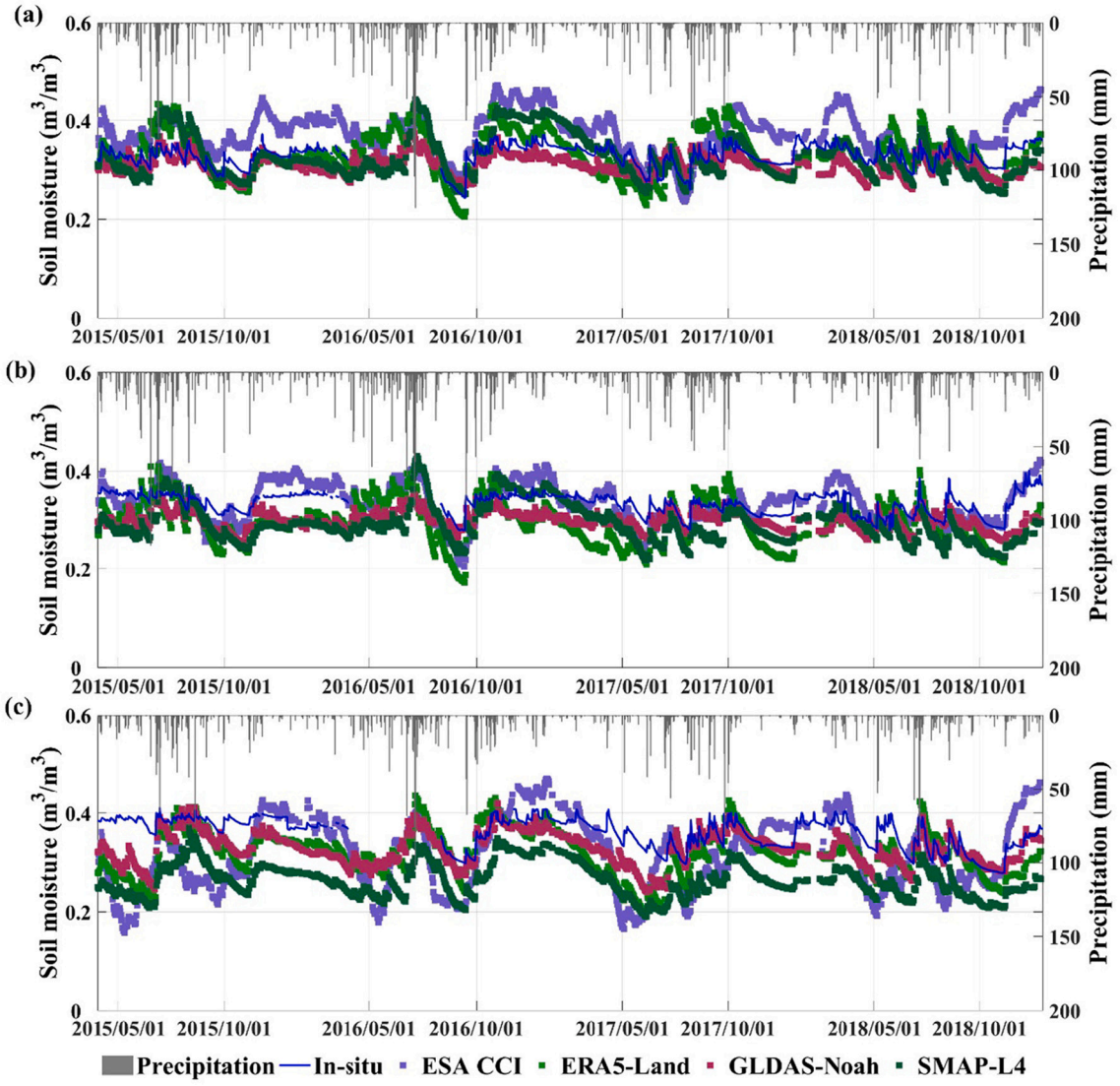

Fig. 8. Time series of the *in situ* RZSM and the four RZSM products for (a) site 58,235, (b) site 58,252 and (c) site M5401 from March 2015 to December 2018 in Jiangsu province. Blue solid lines represent averaged *in situ* measurements. Averaged daily precipitation is represented by grey vertical bars. (For interpretation of the references to colour in this figure legend, the reader is referred to the web version of this article.)

indicating the wet bias of ESA CCI could be resulted from the wet bias of GLDAS Noah SSM as the uncertainty of the GLDAS-Noah model was included during the unit scaling and the TCA hypothetical destruction during ESA CCI SSM's merging scheme (Al-Yaari et al., 2019; Zeng et al., 2022). Thus, the accuracy of the ESA CCI, GLDAS-Noah and ERA5-Land SSM products was expected to be enhanced by considering the water effect.

No significant R between WF and the accuracy of satellite SSM was observed. It could be explained by the fact that some filters related to WF were applied to filter the pixels contaminated by water bodies, though some uncertainties related to water fraction could still exist in some SSM products.

5.1.2. Vegetation optical depth (VOD)

VOD, related to the intensity of microwave extinction effects within the vegetation canopy layer, is often regarded as a vegetation index (Fan et al., 2018; Li et al., 2021). Its accuracy also highly impacted the accuracy of the radiometric SSM retrievals over the vegetated regions (Wigneron et al., 2017).

Table 7 and Fig. S15 showed that the accuracy of the GLDAS-Noah and merged (*i.e.*, ESA CCI and ESA CCI-P) SSM product was significantly positively correlated with VOD with R of 0.23, 0.32 and 0.23, indicating the dense vegetation covers could hardly affect the accuracy of the above SSM products. While the accuracy of the satellite-based SSM products (*i.e.*, MTDCA and SMAP-MCCA) was significantly negatively correlated with VOD with R of −0.46 and − 0.31, suggesting that MTDCA and SMAP-MCCA SSM performed better over sites covered with sparse vegetation than over ones with dense vegetation covers in Jiangsu province. This could be explained that the VOD over dense vegetation layers was higher than that in sparsely vegetated regions, making the impact of the soil signal on the total above-canopy emission smaller and thus SSM retrievals less accurate over dense vegetation covers (Grant et al., 2008).

5.1.3. Radio-frequency interference (RFI)

RFI influences the quantity and quality of TB received by radiometers, influencing the SSM retrievals (Wigneron et al., 2021). Fig. S16 presents the spatial distribution of L-band RFI (in terms of TB-RMSE <8 K) and correlation coefficients (R) between SMOS-IC and *in situ* SSM. The SMOS-IC pixels over most sites had high RFI values, preventing retrievals of high-quality SSM data. Besides, significantly positive R values between SMOS-IC and *in situ* SSM were observed over the region

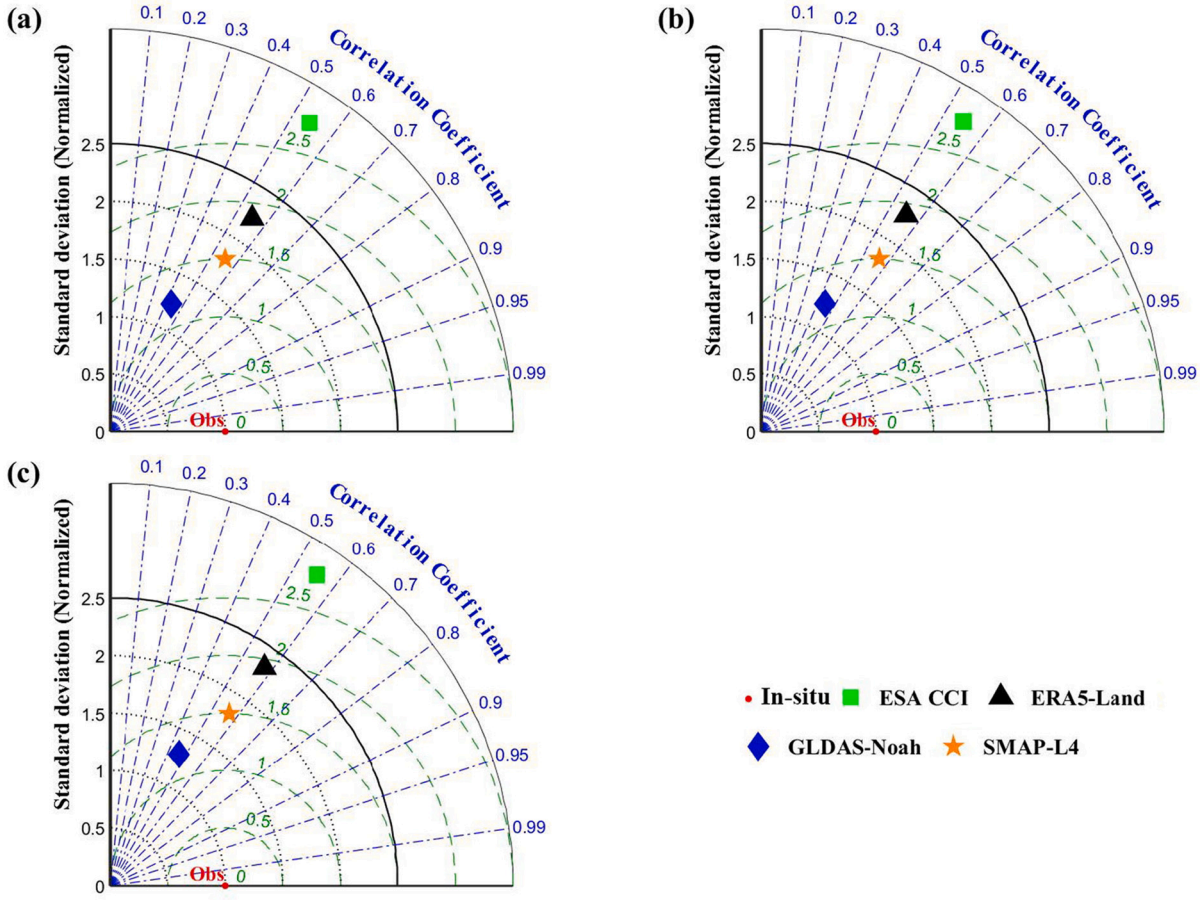

Fig. 9. Taylor's diagrams displaying a statistical comparison between ESA CCI, SMAP-L4, ERA5-Land and GLDAS- Noah RZSM products with *in situ* RZSM during 2015–2018. The green dash lines represent the centered RMSE (cRMSE) values, which distance the 'Obs' point. (a) – (c) show the median error metrics from Case 1 to Case 3, respectively. (For interpretation of the references to colour in this figure legend, the reader is referred to the web version of this article.)

Table 6
Summary median metrics of comparing four RZSM products with *in situ* measurements for each Case. Bias and ubRMSE are both in m^3/m^3. *N* is the average number of samples. The bold font highlights the best results for each error metric.

Cases	Products	bias	ubRMSE	*R*	slope	*N*	Sites
Case 1	ESA CCI	−0.06	0.05	0.54	1.55	1080	78
	ERA5-Land	**−0.04**	0.04	**0.55**	1.23	1154	83
	GLDAS-Noah	−0.05	**0.03**	0.43	0.52	1154	77
	SMAP-L4	−0.08	**0.03**	**0.55**	**0.82**	1154	85
Case 2	ESA CCI	−0.06	0.05	0.55	1.71	1082	75
	ERA5-Land	**−0.04**	0.04	**0.56**	1.27	1154	75
	GLDAS-Noah	−0.05	**0.03**	0.44	0.55	1154	75
	SMAP-L4	−0.08	**0.03**	**0.56**	**0.95**	1154	75
Case 3	ESA CCI	−0.07	0.05	0.55	1.73	1084	73
	ERA5-Land	**−0.04**	0.03	**0.58**	1.31	1084	73
	GLDAS-Noah	−0.06	0.02	0.46	0.58	1084	73
	SMAP-L4	−0.08	**0.01**	0.57	**1.00**	1084	73

Table 7
Summary *R* by comparing the significant *R* (between thirteen SSM products and *in situ* observations) with potential factors (*i.e.*, VOD, and WF). The relationship with significant (*P-Value* < 0.05/0.01, */**) correlation coefficients are shown.

Products	VOD		WF	
	R	*P-Value*	*R*	*P-Value*
ASCAT	−0.05	0.70	0.05	0.75
ESA CCI	0.23*	0.04	−0.20	0.07
ESA CCI-P	0.32**	0.01	−0.05	0.70
ESA CCI-A	0.04	0.77	−0.19	0.11
ERA5-Land	0.18	0.08	−0.43**	0.00
GLDAS-Noah	0.23*	0.03	−0.26*	0.01
SMOS-IC	−0.09	0.63	0.26	0.15
LPRM	0.26	0.10	−0.03	0.86
MTDCA	−0.46**	0.00	0.12	0.36
SMAP-L3	−0.25	0.06	0.20	0.14
SMAP-L4	0.07	0.52	0.00	0.99
SMAP-MCCA	−0.31**	0.01	−0.04	0.75
SMAP-IB	0.09	0.62	−0.17	0.33

having lower RFI values (TB-RMSE <6 K), suggesting that the performance of SMOS-IC SSM could be mainly affected by RFI over Jiangsu province. We also plotted the scatterplots between RFI (*i.e.*, TB-RMSE) and the significant *R* values of SMOS-IC for *in situ* sites (Fig. S17), but no significant *R* between them was observed.

Apart from the above errors, some uncertainties should also not be ignored. For example, the spatial mismatch between *in situ* sites and satellite and model-based products could exist. Besides, differences in the sampling depths among the sensors and products may also bring some uncertainties to the assessment (Li et al., 2022). Nevertheless, despite these limitations, the method used to assess the products is relatively reasonable as 1) all the ninety-one *in situ* sites are evenly distributed throughout Jiangsu province. 2) we considered the *R*, ubRMSE, and cRMSE as the main metrics for the assessment as they are less impacted by the spatial mismatch between *in situ* site and products.

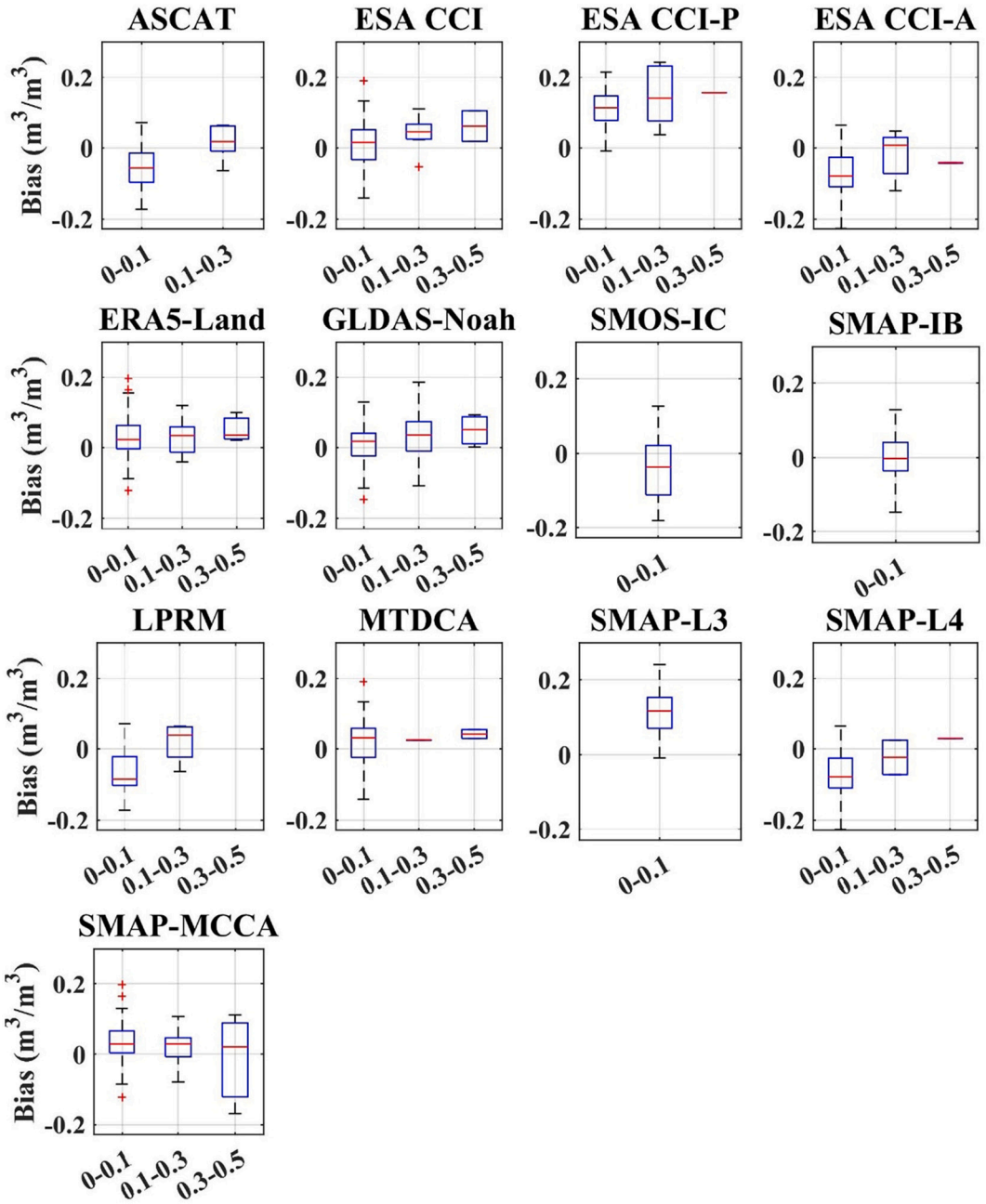

Fig. 10. Box plots of bias for the thirteen SSM products considering WF classifications.

5.2. Influence of the evaluation strategies on the metrics of the SSM and RZSM datasets

Four cases for SSM and three cases for RZSM were used to investigate the influence of the available sites and data samplings on the SSM and RZSM performance metrics in the evaluation, respectively. Overall, all SSM products' performance ranking was generally consistent for Case1-Case3, while slightly better metric scores and different performance were obtained in Case 4 when considering overlapped dates within common sites for all products. For RZSM, all cases have similar performance rankings as they were less affected by the influence of the available sites and data samplings.

Previous studies have shown that the most frequently used evaluation method is Case 1, which uses all available sites and data samplings (*e.g.*, (Al-Yaari et al., 2019; Xing et al., 2021; Zeng et al., 2015)). Case 1 assumes that the potential users may use the SSM or RZSM products separately, hence, each product's actual accuracy was evaluated and presented separately (Al-Yaari et al., 2019). The evaluation results between the SSM and RZSM products with *in situ* measurements from 2011 to 2018 were added in the Supplementary Information (Table S4). However, the method could be biased for some products in the intercomparison, as different sites and dates were used for these products. For instance, SMOS-IC (Sites = 33 and average $N = 110$) has fewer dates and sites than LPRM (Sites = 43 and average $N = 632$) because RFI strongly influenced the former in Jiangsu province (Table 5).

The common sites were used in Case 2 (Sites = 7) and Case 3 (Sites = 18) for SSM by either including or excluding SMOS-IC and SMAP-IB, respectively. Our results showed that the SSM products' performance in the two cases (particularly Case 3) was almost consistent with that in Case 1, suggesting stable accuracy of the SSM products in the two cases due to the low uncertainties in flat areas in Jiangsu province and relatively complete temporal samplings of the products.

Slightly better performances were obtained for SSM and RZSM products in Case 4 and Case 3, respectively, when considering overlapped dates within common sites for all products. This is in line with the results obtained by Al-Yaari et al. (Al-Yaari et al., 2019), reporting increasing *R* when overlapped data points are conducted. This could be partly attributed to a much stricter filtering rule when using collocated data than in the other cases because only the high-quality satellite and model-based SSM and RZSM values were reserved for the evaluation in that case. Thus, a much stricter filtering rule could be applied by combining the quality controls of the different SSM products. Moreover, overlapped dates could be optimal to ensure fair inter-comparisons among different products (Gruber et al., 2020). However, a different performance ranking was obtained for SSM between Case4 and the other three cases, which may be due to the limited availability of the *in situ* sites (only 3 sites) and temporal samplings (only 88 data) that deviated from the evaluation results. Thus, it is important to select appropriate evaluation strategies to conduct the SSM and RZSM evaluations according to the situations.

5.3. Comparisons among the two TCA and in situ-based R

Our evaluation results showed that a similar performance for the SSM products was obtained using time-invariant and time-variant TCA-*R* and *in situ*-based *R* calculated using SSM anomalies, suggesting that the TCA method can be used for the satellite and reanalysis SSM evaluation in the absence of ground truth (Fig. 5). However, the TCA-*R* for the SSM products was consistently higher than the *in situ*-based *R*. This could be due to the *in situ*-based *R* may contain errors associated with the representativeness of the *in situ* sites, as spatial mismatches could exist between the SSM values obtained from *in situ* sites and from remotely sensed reanalysis SSM products with a coarse resolution (Crow et al., 2015; Dong et al., 2020b).

Considering both time-invariant and time-variant TCA-*R* are necessary for accurate SSM retrievals at different time scales over the cropland. Our evaluation results showed that the daily *R* values obtained by time-variant TCA implementation have larger temporal variability than the time-invariant *R* derived from long-term TCA (Fig. 5). This is consistent with the results of previous studies (*e.g.*, (Su et al., 2014); Wu et al. (2021a), *etc.*), which also found large SSM temporal variability at short time scales. This could be attributed to the influence of other factors (*e.g.*, rainfall, vegetation growth, *etc.*) over the whole research period in the croplands, as dense vegetation covers and rainfall increase the difficulty and introduce large uncertainties in retrieving SSM using TB or backscattering coefficients. For example, we compared the median time-variant TCA-*R* at different VOD ranges and found that a decreasing accuracy for the satellite SSM products (*e.g.*, MTDCA, SMAP-MCCA and SMAP-IB) was obtained over the vegetation growth period (VOD $>$ 0.15). This also confirmed our results above that the accuracy of MTDCA and SMAP-MCCA SSM could be affected by the influence of dense vegetation covers (Fig. S18).

6. Conclusions

This study assessed the performance of thirteen SSM and four RZSM datasets using *in situ* measurements under different evaluation strategies in Jiangsu province. We also inter-compared time-invariant, time-variant TCA-*R* and *in situ*-based *R*. The impacts of vegetation and water fraction on the accuracy of the reanalysis and satellite-based SSM products were also investigated. Our conclusions are as follows.

(1) Regarding SSM, the model-based and combined SSM products (*i.e.*, ERA5-Land, SMAP-L4, ESA CCI/ESA CCI-P/ESA CCI-A, GLDAS-Noah) performed better than the active SSM product (*i.e.*, ASCAT), than the passive satellite SSM products (*i.e.*, SMAP-L3, SMOS-IB, SMAP-IC, MTDCA, SMAP-MCCA and LPRM) in Jiangsu province with higher *R* and lower ubRMSE. Similar performance rankings were observed among time-invariant and time-variant TCA-*R* and *in situ*-based *R*, in which the TCA-*R* values for all SSM datasets were higher than the *in situ*-based *R* as the representativeness errors of the *in situ* measurements may bias *in situ*-based *R*. Besides, considering both time-invariant and time-variant TCA-*R* are necessary for accurate SSM retrievals at different time scales.

(2) Regarding RZSM, ERA5-Land, SMAP-L4 and ESA CCI RZSM (retrieved using ESA CCI SSM coupled with an exponential filter) generally performed better than the GLDAS-Noah RZSM product in capturing the temporal evolution of *in situ* RZSM with an average $R > 0.55$ for the former three products *vs.* an average *R* of 0.44 for GLDAS-Noah. All the RZSM products performed well with low median ubRMSE values (ubRMSE $<0.05\ m^3/m^3$).

(3) Both the SSM and RZSM products provided slightly higher scores when the different datasets were temporally collocated, as many strict filtering rules were applied, and it could be regarded as an optimal way to ensure fair comparisons. However, it is important to select appropriate evaluation strategies to conduct the SSM and RZSM evaluations according to the situation as the available sites and temporal samplings may bias the evaluation results.

(4) By exploring the potential errors for the SSM products, we found the accuracy of the ESA CCI, GLDAS-Noah and ERA5-Land SSM products was expected to be enhanced by considering the water effect and large uncertainties were observed for MTDCA and SMAP-MCCA SSM over dense vegetation periods and regions in Jiangsu province. Besides, the limited available data number of SMOS-IC in the study region could be mainly attributed to RFI.

Data availability

The soil moisture observations in Jiangsu province is not publicly available but could be requested from the Jiangsu Meteorological Information Center (http://js.cma.gov.cn/). SMAP-MCCA SSM data is freely available at https://data.tpdc.ac.cn/en/disallow/591bb9c8-ed6f-4e86-8372-de1c39ba0283/. SMOS-IC and SMAP-IB SSM products from this study are freely available from SMOS-IC website (https://ib.remote-sensing.inrae.fr/). MTDCA SSM data is freely available at http://afeldman.mit.edu/mt-dca-data. AMSR2 LPRM SSM product is freely available at https://disc.gsfc.nasa.gov/datasets/LPRM_AMSR2_A_SOILM3_001/summary. SMAP-L3 SSM and VOD data (https://nsidc.org/data/spl3smp/versions/8) and SMAP L4 SSM and RZSM data (https://nsidc.org/data/spl4smgp/versions/6) are freely available from the National Snow & Ice Data Center. ASCAT SSM data is freely available at http://hsaf.meteoam.it/description-h25-h108-h111.php. ESA CCI Combined/Active/Passive SSM data is freely available at http://www.esa-soilmoisture-cci.org. ERA5-Land soil moisture and precipitation products are freely available at https://cds.climate.copernicus.eu/cdsapp#!/dataset/reanalysis-era5-land?tab=overview. GLDAS-Noah SSM and RZSM products are freely available at https://disc.gsfc.nasa.gov/datasets/GLDAS_NOAH025_3H_2.1/summary. IGBP MODIS land cover product is freely available at https://modis.gsfc.nasa.gov/data/dataprod/mod12.php. Additional data used in the paper are publicly available, with their location provided in the respective references.

Credit author statement

L.F., ZP.X., J.-P·W, and XJ.L. designed the study. ZP.X. carried out all calculations with support from XJ.L., XZ.L., MJ.W., and HL.M. XJ.L. prepared the SMOS-IC and SMAP-IB SSM datasets and TJ.Z. prepared the SMAP-MCCA SSM dataset; CX.Y. and GJ.W. provided the *in-situ* measurements in Jiangsu province. ZP.X., L.F., and J.-P·W conducted the analysis with support from GD.L., F.F., J.P., XJ.L., XZ.L. and MJ.W. The manuscript was drafted by ZP.X., L.F., J.-P·W, GD.L., F.F., J.P., XJ.L., JY.Z., K.Y. and TJ.Z. with contributions by all co-authors.

Declaration of Competing Interest

The authors declare that they have no known competing financial interests or personal relationships that could have appeared to influence the work reported in this paper.

Data availability

No data was used for the research described in the article.

Acknowledgements

This study was supported by the National Natural Science Foundation of China (Grant No. 42171339), the Fundamental Research Funds for the Central Universities (SWU020016), and the National Key Research and Development Program of China (2020YFA0608703, 2021YFB3900104).

Appendix A. Supplementary data

Supplementary data to this article can be found online at https://doi.org/10.1016/j.rse.2022.113283.

References

Al-Yaari, A., Wigneron, J.P., Dorigo, W., Colliander, A., Pellarin, T., Hahn, S., Mialon, A., Richaume, P., Fernandez-Moran, R., Fan, L., Kerr, Y.H., De Lannoy, G., 2019. Assessment and inter-comparison of recently developed/reprocessed microwave satellite soil moisture products using ISMN ground-based measurements. Remote Sens. Environ. 224, 289–303.

Al-Yaari, A., Wigneron, J.P., Kerr, Y., de Jeu, R., Rodriguez-Fernandez, N., van der Schalie, R., Al Bitar, A., Mialon, A., Richaume, P., Dolman, A., Ducharne, A., 2016. Testing regression equations to derive long-term global soil moisture datasets from passive microwave observations. Remote Sens. Environ. 180, 453–464.

Albergel, C., de Rosnay, P., Gruhier, C., Muñoz-Sabater, J., Hasenauer, S., Isaksen, L., Kerr, Y., Wagner, W., 2012. Evaluation of remotely sensed and modelled soil moisture products using global ground-based in situ observations. Remote Sens. Environ. 118, 215–226.

Albergel, C., Rudiger, C., Pellarin, T., Calvet, J.-C., Fritz, N., Froissard, F., Suquia, D., Petitpa, A., Piguet, B., Martin, E., 2008. From near-surface to root-zone soil moisture using an exponential filter: an assessment of the method based on in-situ observations and model simulations. Hydrology and Earth System Sciences 12, 1323–1337.

Bi, H., Ma, J., Zheng, W., Zeng, J., 2016. Comparison of soil moisture in GLDAS model simulations and in situ observations over the tibetan plateau. Journal of Geophysical Research: Atmospheres 121, 2658–2678.

Chan, S.K., Bindlish, R., O'Neill, P.E., Njoku, E., Jackson, T., Colliander, A., Chen, F., Burgin, M., Dunbar, S., Piepmeier, J., Yueh, S., Entekhabi, D., Cosh, M.H., Caldwell, T., Walker, J., Wu, X., Berg, A., Rowlandson, T., Pacheco, A., McNairn, H., Thibeault, M., Martinez-Fernandez, J., Gonzalez-Zamora, A., Seyfried, M., Bosch, D., Starks, P., Goodrich, D., Prueger, J., Palecki, M., Small, E.E., Zreda, M., Calvet, J.-C., Crow, W.T., Kerr, Y., 2016. Assessment of the SMAP passive soil moisture product. IEEE Trans. Geosci. Remote Sens. 54, 4994–5007.

Chatterjee, S., Desai, A.R., Zhu, J., Townsend, P.A., Huang, J., 2022. Soil moisture as an essential component for delineating and forecasting agricultural rather than meteorological drought. Remote Sens. Environ. 269, 112833.

Chen, F., Crow, W.T., Bindlish, R., Colliander, A., Burgin, M.S., Asanuma, J., Aida, K., 2018a. Global-scale evaluation of SMAP, SMOS and ASCAT soil moisture products using triple collocation. Remote Sens. Environ. 214, 1–13.

Chen, J., Sun, X., Tang, H., Fei, Q., Shen, Z., 2018b. Comparative analysis of soil moisture observations and reanalysis in Jiangsu Province. J. Meteorol. Sci. 38, 523–530.

Chen, Y., Yang, K., Qin, J., Zhao, L., Tang, W., Han, M., 2013. Evaluation of AMSR-E retrievals and GLDAS simulations against observations of a soil moisture network on the central tibetan plateau. Journal of Geophysical Research: Atmospheres 118, 4466–4475.

Chen, Y., Yuan, H., 2020. Evaluation of nine sub-daily soil moisture model products over China using high-resolution in situ observations. J. Hydrol. 588.

Cho, E., Choi, M., Wagner, W., 2015. An assessment of remotely sensed surface and root zone soil moisture through active and passive sensors in Northeast Asia. Remote Sens. Environ. 160, 166–179.

Cho, E., Su, C.-H., Ryu, D., Kim, H., Choi, M., 2017. Does AMSR2 produce better soil moisture retrievals than AMSR-E over Australia? Remote Sens. Environ. 188, 95–105.

Crow, W.T., Lei, F., Hain, C., Anderson, M.C., Scott, R.L., Billesbach, D., Arkebauer, T., 2015. Robust estimates of soil moisture and latent heat flux coupling strength obtained from triple collocation. Geophys. Res. Lett. 42, 8415–8423.

Dong, J., Crow, W.T., 2017. An improved triple collocation analysis algorithm for decomposing autocorrelated and white soil moisture retrieval errors. J. Geophys. Res. Atmos. 122, 13,081–13,094.

Dong, J., Crow, W.T., Tobin, K.J., Cosh, M.H., Bosch, D.D., Starks, P.J., Seyfried, M., Collins, C.H., 2020a. Comparison of microwave remote sensing and land surface modeling for surface soil moisture climatology estimation. Remote Sens. Environ. 242.

Dong, J., Lei, F., Wei, L., 2020b. Triple collocation based multi-source precipitation merging. FrontiersWater 2.

Dorigo, W., Wagner, W., Albergel, C., Albrecht, F., Balsamo, G., Brocca, L., Chung, D., Ertl, M., Forkel, M., Gruber, A., Haas, E., Hamer, P.D., Hirschi, M., Ikonen, J., de Jeu, R., Kidd, R., Lahoz, W., Liu, Y.Y., Miralles, D., Mistelbauer, T., Nicolai-Shaw, N., Parinussa, R., Pratola, C., Reimer, C., van der Schalie, R., Seneviratne, S.I., Smolander, T., Lecomte, P., 2017. ESA CCI soil moisture for improved earth system understanding: state-of-the art and future directions. Remote Sens. Environ. 203, 185–215.

Draper, C., Reichle, R., de Jeu, R., Naeimi, V., Parinussa, R., Wagner, W., 2013. Estimating root mean square errors in remotely sensed soil moisture over continental scale domains. Remote Sens. Environ. 137, 288–298.

Entekhabi, D., Njoku, E.G., O'Neill, P.E., Kellogg, K.H., Crow, W.T., Edelstein, W.N., Entin, J.K., Goodman, S.D., Jackson, T.J., Johnson, J., Kimball, J., Piepmeier, J.R., Koster, R.D., Martin, N., McDonald, K.C., Moghaddam, M., Moran, S., Reichle, R., Shi, J.C., Spencer, M.W., Thurman, S.W., Tsang, L., Van Zyl, J., 2010. The soil moisture active passive (SMAP) Mission. Proc. IEEE 98, 704–716.

Fan, L., Wigneron, J.P., Xiao, Q., Al-Yaari, A., Wen, J., Martin-StPaul, N., Dupuy, J.L., Pimont, F., Al Bitar, A., Fernandez-Moran, R., Kerr, Y.H., 2018. Evaluation of microwave remote sensing for monitoring live fuel moisture content in the Mediterranean region. Remote Sens. Environ. 205, 210–223.

Fan, L., Xiao, Q., Wen, J., Liu, Q., Jin, R., You, D., Li, X., 2015. Mapping high-resolution soil moisture over heterogeneous cropland using multi-resource remote sensing and ground observations. Remote Sens. 7, 13273–13297.

Friedl, M., Sulla-Menashe, D., 2019. MCD12Q1 MODIS/Terra+Aqua Land Cover Type Yearly L3 Global 500m SIN Grid V006 [Data set]. NASA EOSDIS Land Processes DAAC. https://doi.org/10.5067/MODIS/MCD12Q1.006. Accessed 2021-02-17 from.

Gao, X., Zhao, X., Brocca, L., Huo, G., Lv, T., Wu, P., 2017. Depth scaling of soil moisture content from surface to profile: multistation testing of observation operators. Hydrogeol. Earth Syst.Sci. 1–25.

González-Zamora, Á., Sánchez, N., Martínez-Fernández, J., Wagner, W., 2016. Root-zone plant available water estimation using the SMOS-derived soil water index. Adv. Water Resour. 96, 339–353.

Gouweleeuw, B.T., van Dijk, A.I.J.M., Guerschman, J.P., Dyce, P., Owe, M., 2012. Space-based passive microwave soil moisture retrievals and the correction for a dynamic open water fraction. Hydrol. Earth Syst. Sci. 16, 1635–1645.

Grant, J.P., Saleh-Contell, K., Wigneron, J.P., Guglielmetti, M., Kerr, Y.H., Schwank, M., Skou, N., Van de Griend, A.A., 2008. Calibration of the L-MEB model over a coniferous and a deciduous forest. IEEE Trans. Geosci. Remote Sens. 46, 808–818.

Gruber, A., De Lannoy, G., Albergel, C., Al-Yaari, A., Brocca, L., Calvet, J.C., Colliander, A., Cosh, M., Crow, W., Dorigo, W., Draper, C., Hirschi, M., Kerr, Y., Konings, A., Lahoz, W., McColl, K., Montzka, C., Muñoz-Sabater, J., Peng, J., Reichle, R., Richaume, P., Rüdiger, C., Scanlon, T., van der Schalie, R., Wigneron, J. P., Wagner, W., 2020. Validation practices for satellite soil moisture retrievals: what are (the) errors? Remote Sens. Environ. 244.

Gruber, A., Su, C.H., Crow, W.T., Zwieback, S., Dorigo, W.A., Wagner, W., 2016. Estimating error cross-correlations in soil moisture data sets using extended collocation analysis. J. Geophys. Res. Atmos. 121, 1208–1219.

Hirschi, M., Seneviratne, S.I., Alexandrov, V., Boberg, F., Boroneant, C., Christensen, O. B., Formayer, H., Orlowsky, B., Stepanek, P., 2010. Observational evidence for soil-moisture impact on hot extremes in southeastern Europe. Nat. Geosci. 4, 17–21.

Hu, G., Zhao, L., Zhu, X., Wu, X., Wu, T., Li, R., Xie, C., Hao, J., 2020. Review of algorithms and parameterizations to determine unfrozen water content in frozen soil. Geoderma 368.

Jackson, T.J., Schmugge, J., Engman, E.T., 2009. Remote sensing applications to hydrology: soil moisture. Hydrol. Sci. J. 41, 517–530.

Jia, B., Liu, J., Xie, Z., 2015. Evaluation of a multi-satellite soil moisture product and the community land model 4.5 simulation in China. Hydrogeol. Earth Syst.Sci. 12, 5151–5186.

Kerr, Y.H., Waldteufel, P., Wigneron, J.-P., Delwart, S., Cabot, F., Boutin, J., Escorihuela, M.-J., Font, J., Reul, N., Gruhier, C., Juglea, S.E., Drinkwater, M.R., Hahne, A., Martín-Neira, M., Mecklenburg, S., 2010. The SMOS Mission: new tool for monitoring key elements ofthe global water cycle. Proc. IEEE 98, 666–687.

Kim, H., Parinussa, R., Konings, A.G., Wagner, W., Cosh, M.H., Lakshmi, V., Zohaib, M., Choi, M., 2018. Global-scale assessment and combination of SMAP with ASCAT (active) and AMSR2 (passive) soil moisture products. Remote Sens. Environ. 204, 260–275.

Kim, H., Wigneron, J.-P., Kumar, S., Dong, J., Wagner, W., Cosh, M.H., Bosch, D.D., Collins, C.H., Starks, P.J., Seyfried, M., Lakshmi, V., 2020. Global scale error assessments of soil moisture estimates from microwave-based active and passive satellites and land surface models over forest and mixed irrigated/dryland agriculture regions. Remote Sens. Environ. 251.

Koike, T., Nakamura, Y., Kaihotsu, I., Davaa, G., Matsuura, N., Tamagawa, K., Fujii, H., 2004. Development of an advanced microwave scanning radiometer (AMSR-E) algorithm of soil moisture and vegetation water content. Proc. Hydraul. Eng. 48, 217–222.

Konings, A.G., Piles, M., Das, N., Entekhabi, D., 2017. L-band vegetation optical depth and effective scattering albedo estimation from SMAP. Remote Sens. Environ. 198, 460–470.

Leroux, D.J., Kerr, Y.H., Richaume, P., Fieuzal, R., 2013. Spatial distribution and possible sources of SMOS errors at the global scale. Remote Sens. Environ. 133, 240–250.
Li, R., Zhao, L., Ding, Y., Wu, T., Xiao, Y., Du, E., Liu, G., Qiao, Y., 2012. Temporal and spatial variations of the active layer along the Qinghai-Tibet highway in a permafrost region. Chin. Sci. Bull. 57, 4609–4616.
Li, X., Al-Yaari, A., Schwank, M., Fan, L., Frappart, F., Swenson, J., Wigneron, J.P., 2020. Compared performances of SMOS-IC soil moisture and vegetation optical depth retrievals based on tau-omega and two-stream microwave emission models. Remote Sens. Environ. 236.
Li, X., Wigneron, J.-P., Fan, L., Frappart, F., Yueh, S.H., Colliander, A., Ebtehaj, A., Gao, L., Fernandez-Moran, R., Liu, X., Wang, M., Ma, H., Moisy, C., Ciais, P., 2022. A new SMAP soil moisture and vegetation optical depth product (SMAP-IB): algorithm, assessment and inter-comparison. Remote Sens. Environment 271.
Li, X., Wigneron, J.-P., Frappart, F., Fan, L., Ciais, P., Fensholt, R., Entekhabi, D., Brandt, M., Konings, A.G., Liu, X., Wang, M., Al-Yaari, A., Moisy, C., 2021. Global-scale assessment and inter-comparison of recently developed/reprocessed microwave satellite vegetation optical depth products. Remote Sens. Environ. 253.
Ling, X., Huang, Y., Guo, W., Wang, Y., Chen, C., Qiu, B., Ge, J., Qin, K., Xue, Y., Peng, J., 2021. Comprehensive evaluation of satellite-based and reanalysis soil moisture products using in situ observations over China. Hydrol. Earth Syst. Sci. 25, 4209–4229.
Luo, M., Sa, C., Meng, F., Duan, Y., Liu, T., Bao, Y., 2020. Assessing remotely sensed and reanalysis products in characterizing surface soil moisture in the mongolian plateau. Int. J. Digit. Earth 14, 1255–1272.
Martens, B., Miralles, D.G., Lievens, H., van der Schalie, R., de Jeu, R.A.M., Fernández-Prieto, D., Beck, H.E., Dorigo, W.A., Verhoest, N.E.C., 2017. GLEAM v3: satellite-based land evaporation and root-zone soil moisture. Geosci. Model Dev. 10, 1903–1925.
McColl, K.A., Vogelzang, J., Konings, A.G., Entekhabi, D., Piles, M., Stoffelen, A., 2014. Extended triple collocation: estimating errors and correlation coefficients with respect to an unknown target. Geophys. Res. Lett. 41, 6229–6236.
Miralles, D.G., van den Berg, M.J., Gash, J.H., Parinussa, R.M., de Jeu, R.A.M., Beck, H. E., Holmes, T.R.H., Jiménez, C., Verhoest, N.E.C., Dorigo, W.A., Teuling, A.J., Johannes Dolman, A., 2013. El Niño–La Niña cycle and recent trends in continental evaporation. Nat. Clim. Chang. 4, 122–126.
Muñoz-Sabater, J., Dutra, E., Agustí-Panareda, A., Albergel, C., Arduini, G., Balsamo, G., Boussetta, S., Choulga, M., Harrigan, S., Hersbach, H., Martens, B., Miralles, D.G., Piles, M., Rodríguez-Fernández, N.J., Zsoter, E., Buontempo, C., Thépaut, J.N., 2021. ERA5-land: a state-of-the-art global reanalysis dataset for land applications. Earth Syst. Sci. Data 13, 4349–4383.
Njoku, E.G., Ashcroft, P., Chan, T.K., Li, L., 2005. Global survey and statistics of radio-frequency interference in AMSR-E land observations. IEEE Trans. Geosci. Remote Sens. 43, 938–947.
Ochsner, E., Cosh, M.H., Cuenca, R., Hagimoto, Y., Kerr, Y.H., Njoku, E., Zreda, M., 2013. State of the art in large-scale soil moisture monitoring. Soil Sci. Soc. Am. J. 1–32.
Owe, M., de Jeu, R., Holmes, T., 2008. Multisensor historical climatology of satellite-derived global land surface moisture. J. Geophys. Res. 113.
Paulik, C., Dorigo, W., Wagner, W., Kidd, R., 2014. Validation of the ASCAT soil water index using in situ data from the international soil moisture network. Int. J. Appl. Earth Obs. Geoinf. 30, 1–8.
Peng, J., Albergel, C., Balenzano, A., Brocca, L., Cartus, O., Cosh, M.H., Crow, W.T., Dabrowska-Zielinska, K., Dadson, S., Davidson, M.W.J., de Rosnay, P., Dorigo, W., Gruber, A., Hagemann, S., Hirschi, M., Kerr, Y.H., Lovergine, F., Mahecha, M.D., Marzahn, P., Mattia, F., Musial, J.P., Preuschmann, S., Reichle, R.H., Satalino, G., Silgram, M., van Bodegom, P.M., Verhoest, N.E.C., Wagner, W., Walker, J.P., Wegmüller, U., Loew, A., 2021. A roadmap for high-resolution satellite soil moisture applications – confronting product characteristics with user requirements. Remote Sens. Environ. 252.
Peng, J., Niesel, J., Loew, A., Zhang, S., Wang, J., 2015. Evaluation of satellite and reanalysis soil moisture products over Southwest China using ground-based measurements. Remote Sens. 7.
Reichle, R.H., De Lannoy, G.J.M., Liu, Q., Ardizzone, J.V., Colliander, A., Conaty, A., Crow, W., Jackson, T.J., Jones, L.A., Kimball, J.S., Koster, R.D., Mahanama, S.P., Smith, E.B., Berg, A., Bircher, S., Bosch, D., Caldwell, T.G., Cosh, M., González-Zamora, Á., Holifield Collins, C.D., Jensen, K.H., Livingston, S., Lopez-Baeza, E., Martínez-Fernández, J., McNairn, H., Moghaddam, M., Pacheco, A., Pellarin, T., Prueger, J., Rowlandson, T., Seyfried, M., Starks, P., Su, Z., Thibeault, M., van der Velde, R., Walker, J., Wu, X., Zeng, Y., 2017. Assessment of the SMAP Level-4 surface and root-zone soil moisture product using in situ measurements. J. Hydrometeorol. 18, 2621–2645.
Reichle, R.H., Koster, R.D., Liu, P., Mahanama, S.P.P., Njoku, E.G., Owe, M., 2007. Comparison and assimilation of global soil moisture retrievals from the advanced microwave scanning radiometer for the earth observing system (AMSR-E) and the scanning multichannel microwave radiometer (SMMR). J. Geophys. Res. 112.
Rodell, M., Houser, P.R., Jambor, U., Gottschalck, J., Mitchell, K., Meng, C.-J., Arsenault, K., Cosgrove, B., Radakovick, J., Bosilovich, M., Entin, J.K., Walker, J.P., Lohmann, D., Toll, D., 2004. The global land data assimilation system. Bull. Amer. Meteor. Soc. 85, 381–394.
Rossini, P., Patrignani, A., 2021. Predicting rootzone soil moisture from surface observations in cropland using an exponential filter. Soil Sci. Soc. Am. J. 85, 1894–1902.
Seneviratne, S.I., Corti, T., Davin, E.L., Hirschi, M., Jaeger, E.B., Lehner, I., Orlowsky, B., Teuling, A.J., 2010. Investigating soil moisture–climate interactions in a changing climate: a review. Earth Sci. Rev. 99, 125–161.
Su, C.-H., Ryu, D., Crow, W.T., Western, A.W., 2014. Stand-alone error characterisation of microwave satellite soil moisture using a fourier method. Remote Sens. Environ. 154, 115–126.
Sun, Y., Huang, S., Ma, J., Li, J., Li, X., Wang, H., Chen, S., Zang, W., 2017. Preliminary evaluation of the SMAP radiometer soil moisture product over China using in situ data. Remote Sens. 9.
Taylor, K.E., 2001. Summarizing multiple aspects of model performance in a single diagram. J. Geophys. Res. Atmos. 106, 7183–7192.
Wagner, W., Hahn, S., Kidd, R., Melzer, T., Bartalis, Z., Hasenauer, S., Figa-Saldaña, J., de Rosnay, P., Jann, A., Schneider, S., Komma, J., Kubu, G., Brugger, K., Aubrecht, C., Züger, J., Gangkofner, U., Kienberger, S., Brocca, L., Wang, Y., Blöschl, G., Eitzinger, J., Steinnocher, K., 2013. The ASCAT soil moisture product: a review of its specifications, validation results, and emerging applications. Meteorol. Z. 22, 5–33.
Wagner, W., Lemoine, G., Rott, H., 1999. A method for estimating soil Moisture from ERS scatterometer and soil data. Remote Sens. Environ. 70, 191–207.
Wang, S., Mo, X., Liu, S., Lin, Z., Hu, S., 2016. Validation and trend analysis of ECV soil moisture data on cropland in North China plain during 1981–2010. Int. J. Appl. Earth Obs. Geoinf. 48, 110–121.
Wang, T., Franz, T.E., You, J., Shulski, M.D., Ray, C., 2017. Evaluating controls of soil properties and climatic conditions on the use of an exponential filter for converting near surface to root zone soil moisture contents. J. Hydrol. 548, 683–696.
Wang, Z., Che, T., Zhao, T., Dai, L., Li, X., Wigneron, J.-P., 2021. Evaluation of SMAP, SMOS, and AMSR2 soil moisture products based on distributed ground observation network in cold and arid regions of China. IEEE J. Sel. Top. Appl. Earth Obs. Remote Sens. 14, 8955–8970.
Watson, A., Miller, J., Künne, A., Kralisch, S., 2022. Using soil-moisture drought indices to evaluate key indicators of agricultural drought in semi-arid Mediterranean southern Africa. Sci. Total Environ. 812, 152464.
Wigneron, J.-P., Li, X., Frappart, F., Fan, L., Al-Yaari, A., De Lannoy, G., Liu, X., Wang, M., Le Masson, E., Moisy, C., 2021. SMOS-IC data record of soil moisture and L-VOD: historical development, applications and perspectives. Remote Sens. Environ. 254.
Wigneron, J.P., Jackson, T.J., O'Neill, P., De Lannoy, G., de Rosnay, P., Walker, J.P., Ferrazzoli, P., Mironov, V., Bircher, S., Grant, J.P., Kurum, M., Schwank, M., Munoz-Sabater, J., Das, N., Royer, A., Al-Yaari, A., Al Bitar, A., Fernandez-Moran, R., Lawrence, H., Mialon, A., Parrens, M., Richaume, P., Delwart, S., Kerr, Y., 2017. Modelling the passive microwave signature from land surfaces: A review of recent results and application to the L-band SMOS & SMAP soil moisture retrieval algorithms. Remote Sens. Environ. 192, 238–262.
Wu, K., Ryu, D., Nie, L., Shu, H., 2021a. Time-variant error characterization of SMAP and ASCAT soil moisture using Triple Collocation Analysis. Remote Sens. Environ. 256.
Wu, Z., Feng, H., He, H., Zhou, J., Zhang, Y., 2021b. Evaluation of Soil Moisture Climatology and Anomaly Components Derived From ERA5-Land and GLDAS-2.1 in China. Water Resour. Manag. 35, 629–643.
Xing, Z., Fan, L., Zhao, L., De Lannoy, G., Frappart, F., Peng, J., Li, X., Zeng, J., Al-Yaari, A., Yang, K., Zhao, T., Shi, J., Wang, M., Liu, X., Hu, G., Xiao, Y., Du, E., Li, R., Qiao, Y., Shi, J., Wen, J., Ma, M., Wigneron, J.-P., 2021. A first assessment of satellite and reanalysis estimates of surface and root-zone soil moisture over the permafrost region of Qinghai-Tibet Plateau. Remote Sens. Environ. 265.
Xu, L., Chen, N., Zhang, X., Moradkhani, H., Zhang, C., Hu, C., 2021. In-situ and triple-collocation based evaluations of eight global root zone soil moisture products. Remote Sens. Environ. 254, 112248.
Xu, X., Gao, P., Zhu, X., Guo, W., Ding, J., Li, C., 2018. Estimating the responses of winter wheat yields to moisture variations in the past 35 years in Jiangsu Province of China. PLoS One 13, e0191217.
Yang, Q., Zhao, T., Shi, J., Peng, Z., Ye, C., 2021a. A simulation-based approach for removing the effect of water contamination on SMAP soil moisture retrieval over the Qinghai-Tibet Plateau. Remote Sens. Lett. 12, 757–767.
Yang, S., Li, R., Wu, T., Hu, G., Xiao, Y., Du, Y., Zhu, X., Ni, J., Ma, J., Zhang, Y., Shi, J., Qiao, Y., 2020. Evaluation of reanalysis soil temperature and soil moisture products in permafrost regions on the Qinghai-Tibetan Plateau. Geoderma 377.
Yang, Y., Zhang, J., Bao, Z., Ao, T., Wang, G., Wu, H., Wang, J., 2021b. Evaluation of multi-source soil moisture datasets over central and eastern agricultural area of China using in situ monitoring network. Remote Sens. 13.
Zeng, J., Li, Z., Chen, Q., Bi, H., Qiu, J., Zou, P., 2015. Evaluation of remotely sensed and reanalysis soil moisture products over the Tibetan Plateau using in-situ observations. Remote Sens. Environ. 163, 91–110.
Zeng, J., Shi, P., Chen, K.S., Ma, H., Bi, H., Cui, C., 2022. Assessment and error analysis of satellite soil moisture products over the third pole. IEEE Trans. Geosci. Remote Sens. 60, 1–18.
Zhao, T., Shi, J., Bindlish, R., Jackson, T.J., Kerr, Y.H., Cosh, M.H., Cui, Q., Li, Y., Xiong, C., Che, T., 2015. Refinement of SMOS multiangular brightness temperature toward soil moisture retrieval and its analysis over reference targets. IEEE J. Sel. Top. Appl. Earth Obse. Remote Sens. 8, 589–603.
Zhao, T., Shi, J., Entekhabi, D., Jackson, T.J., Hu, L., Peng, Z., Yao, P., Li, S., Kang, C.S., 2021. Retrievals of soil moisture and vegetation optical depth using a multi-channel collaborative algorithm. Remote Sens. Environ. 257.
Zhao, T., Shi, J., Lv, L., Xu, H., Chen, D., Cui, Q., Jackson, T.J., Yan, G., Jia, L., Chen, L., Zhao, K., Zheng, X., Zhao, L., Zheng, C., Ji, D., Xiong, C., Wang, T., Li, R., Pan, J., Wen, J., Yu, C., Zheng, Y., Jiang, L., Chai, L., Lu, H., Yao, P., Ma, J., Lv, H., Wu, J., Zhao, W., Yang, N., Guo, P., Li, Y., Hu, L., Geng, D., Zhang, Z., 2020. Soil moisture experiment in the Luan River supporting new satellite mission opportunities. Remote Sens. Environ. 240.
Zheng, J., Zhao, T., Lü, H., Shi, J., Cosh, M.H., Ji, D., Jiang, L., Cui, Q., Lu, H., Yang, K., Wigneron, J.-P., Li, X., Zhu, Y., Hu, L., Peng, Z., Zeng, Y., Wang, X., Kang, C.S., 2022.

Assessment of 24 soil moisture datasets using a new in situ network in the Shandian River Basin of China. Remote Sens. Environ. 271.